

1 **Computational applications in masonry structures:** 2 **from the meso-scale to the super-large/super-complex**

3 Paulo B. Lourenço¹, Luís C. Silva²

4 ¹ Full Professor, Dept. of Civil Engineering, ISISE, University of Minho, Azurém, 4800-058
5 Guimarães, Portugal. E-mail: pbl@civil.uminho.pt

6 ² Ph.D. candidate, Dept. of Civil Engineering, ISISE, University of Minho, Azurém, 4800-058
7 Guimarães, Portugal. E-mail: luisilva.civil@gmail.com

8 **Abstract**

9 Masonry structures constitute a large portion of the built heritage around the world, from the past and
10 still today. Therefore, understanding their structural behavior is crucial for preserving the historical
11 characteristics of many of those buildings and in addressing the requirements for housing and
12 sustainable development. Due to its composite and highly non-linear nature, the analysis of masonry
13 structures has been a challenge for engineers.

14 This paper presents a set of advanced models for the mechanical study of masonry, including the usual
15 micro-modeling approaches (in which masonry constituents, i.e. unit and joint, are represented
16 separately), macro-modeling (in which masonry constituents are smeared in a homogeneous composite)
17 and multi-scale techniques (in which upscaling from micro to macro is adopted). An extensive overview
18 of its computational features is provided.

19 Finally, the engineering application of such strategies is presented and covers problems from the
20 masonry components level (meso-scale) to the structural element itself, and ultimately to the level of
21 monumental buildings (super-large). The structural safety assessment and/or strengthening schemes
22 evaluation are performed amid the static, slow dynamics or earthquakes, and fast dynamics or impact
23 and blast ranges.

24 **Keywords:** Masonry, Micro-modeling, Macro-modeling, Multi-scale, Homogenization, URM
25 Applications, Seismic load, Fast dynamics, Out-of-plane.

26 **1 Introduction**

27 Masonry is an ancient but still widely used material. Its usage has been mainly fostered by the simplicity
28 of this type of construction, where masonry units are laid together with or without the use of bonding
29 mortar. Features such as its durability, aesthetics, low maintenance, adaptability, good sound and
30 thermal insulation properties (Hendry 2001) are also important allowing the masonry to continuously
31 find an application. Unreinforced masonry (URM) buildings are a relevant part of the worldwide
32 building stock. These include stone, brick, adobe or earthen masonry structures and represent, in
33 countries such as Mexico, Pakistan, and Peru, more than 75% over its total buildings' inventory. In
34 other countries as Iran, Australia, Indonesia or Italy, the relative percentage is higher than 50% (Frankie
35 et al. 2013). A similar trend is found for the case of Portugal, with a value ranging the 50% according
36 to the Portuguese Census of Population and Housing.

37 The widespread of most of this built heritage has been achieved based on empirical knowledge passed
38 by generation to generation and, therefore, the structural behavior of URM was often ill-understood.
39 These constructions have been typically made to withstand vertical loads and its low strength/mass ratio
40 makes them rather vulnerable to dynamic horizontal loads as earthquakes, impact or blast actions. This
41 addresses the importance of carrying out urgent measures in the URM built stock to avoid human and
42 societal consequences and to minimize future economic impacts. Yet, intervening in these constructions
43 is a complex process, due to the lack of structural information and due to their high importance. A
44 scientifically based process is less susceptible to inadequate actions, which clearly sets a convenient
45 context for the continuous development of numerical strategies.

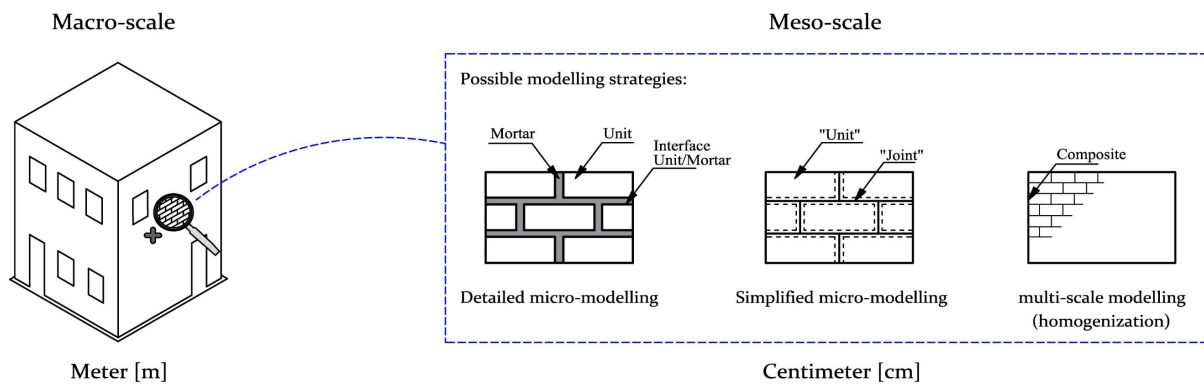
46 Advanced computational strategies have been developed in the last few decades. Conversely to concrete
47 and steel structures, the design guidelines for masonry did not go always hand in hand with the
48 application of innovative methods. Still, it is nowadays well accepted that sophisticated strategies,
49 mainly based on the finite element (FE) method, constitute important tools and are the ones deserving
50 more attention from the scientific community. Three main modeling strategies for the mechanical study
51 of masonry can be put together, namely: (i) the direct numerical simulation or micro-modeling
52 approaches (in which masonry constituents, i.e. unit and joint, are represented separately); (ii) the

53 macro-modeling (in which masonry constituents are smeared in a homogeneous composite); and (iii)
54 the multi-scale techniques (in which upscaling from the meso-scale to the macro-scale is adopted). The
55 mechanical complexity of masonry may demand, in some cases, more detailed analysis with a focus on
56 the components level. Although accurate, a direct numerical simulation (micro-modeling) is expensive
57 to carry out from a computational standpoint and, therefore, macro- or multi-scale techniques can be
58 more appropriate for large or super-large problems. An engineering compromise between the solution
59 accuracy and the time-cost demand needs to be assumed which, depending on the nature of the problem,
60 may constitute a real challenge.

61 **2 General scope**

62 Prevailing design rules or analytical approaches still are, within engineering practice, the most useful
63 towards the structural analysis of URM buildings. These pose, however, several well-identified
64 limitations that may lead to potential unrealistic or conservative results (Theodossopoulos and Sinha
65 2013). Other simplified procedures, as the story-mechanism (Tomažević 1999) and the equivalent
66 frame-based models (Lagomarsino et al. 2013; Quagliarini and Maracchini 2017) can also be found in
67 the literature. Such models, however, hardly consider the out-of-plane failure modes and thus these are
68 generally disregarded in most study cases. More suitable and yet conceptually simple procedures, as
69 the rigid-body approaches (D'Ayala and Shi 2011; Konstantinidis and Makris 2007) or the well
70 disseminated kinematic methods (D'Ayala and Speranza 2003; Griffith and Magenes 2003; Calvi et al.
71 2006), are useful to provide closed-form solutions under dynamic excitations but are very complex for
72 walls subjected to two-way bending.

73 Sophisticated FE computational strategies are the ones which deserve more attention from the scientific
74 community. Several advances have been achieved in the last few decades and these constitute important
75 (sometimes indispensable) analysis tools. For the masonry field, it is recognizable that two scale levels
76 are of interest when analyzing its structural behavior (Paulo B. Lourenço 2009; Roca et al. 2010), the
77 macro- and the meso-scales as depicted in Fig. 1. Again, three main modeling strategies can be put
78 together, namely: (i) the direct simulation or the micro-modeling; (ii) the macro-modeling; and (iii) the
79 multi-scale modeling.



80

Meter [m]

Centimeter [cm]

81 Fig. 1 – Representation of the three scales considered in the analysis of masonry for this study: macro-
 82 scale and meso-scale. Definition of the modeling strategies adopted to represent masonry.

83 In the micro-modeling approach, both masonry components (units and mortar joints) are explicitly
 84 represented. These are certainly capable of well reproducing both in- and out-of-plane orthotropic
 85 nonlinear behavior of masonry but are characterized by long processing times, being only recommended
 86 for limited size structural problems (Giambanco and Rizzo 2001; Macorini and Izzuddin 2011; Lotfi
 87 and Shing 1994; Macorini and Izzuddin 2013; Sejnoha et al. 2008; Lemos 2007; Sarhosis et al. 2014;
 88 Adam et al. 2010). The macro-modeling strategies smear out the heterogeneous assemblage of mortar
 89 and bricks into a fictitious homogeneous anisotropic material. The use of closed-form laws to represent
 90 the complex phenomenological behavior and damage of the masonry may be cumbersome as it may
 91 require a calibration step (usually achieved by thorough experimental campaigns). However, this
 92 approach allows studying large-scale structures without the drawbacks exhibited by meso-modeling
 93 (Dhanasekar et al. 1985; Paulo B. Lourenço et al. 1997; Berto et al. 2002; Roca et al. 2013).

94 Multi-scale FE (or FE²) methods are in-between the latter two FE modeling schemes. The framework
 95 is being used to investigate the response of composites with different natures, see (Spahn et al. 2014;
 96 Leonetti et al. 2018; Trovalusci et al. 2015; Greco et al. 2017). It typically relies on a meso and macro
 97 transition of information and is, therefore, designated as two-scale or FE² approaches. Full continuum-
 98 based FE² approaches result in a good compromise between solution accuracy and computational cost.
 99 Nevertheless, these methods still constitute a challenge if one desires to account for the material non-
 100 linearity (Otero et al. 2015; Geers et al. 2010). In fact, the constant need of data between the macro-
 101 and meso- scales constitute a contentious issue, because a new boundary value problem (BVP) must be

102 solved numerically for each load step and in each Gauss integration point. The utility of the approach
103 is compromised due to the involved computational time and thus full continuum-based FE² approaches
104 are seldom used for dynamic purposes or for complex structural analysis. An adequate possibility is the
105 use of a two-scale simplified strategy, for instance by using a kinematic theorem of limit analysis at a
106 macro-level to obtain the homogenized failure surfaces with a very limited computational effort (A.
107 Cecchi and Milani 2008; Milani et al. 2006; de Buhan and de Felice 1997). Yet, the use of discrete FE-
108 based methods at a macro-level seems to be a promising alternative (Milani and Tralli 2011; Casolo
109 and Milani 2010; Silva et al. 2017b).

110 In this context, three advanced FE-based models, for which the authors gave their contribution, are
111 hereafter addressed and each one belongs to one of the aforementioned modeling strategies (Fig. 1): a
112 simplified micro-model; a macro-model; and a simplified two-scale (FE²) model. Note that the
113 strategies can handle the masonry full softening behavior, anisotropy and its strain-rate dependency
114 under fast dynamic cases. Furthermore, all the strategies have been implemented in advanced FE
115 software's.

116 **3 Modeling strategies proposed**

117 **3.1 FE mesoscopic model**

118 An FE mesoscopic model firstly introduced by (Lourenço 1996) within the so-called simplified micro-
119 modeling approach is presented next. The interface model for masonry has the ability to reproduce the
120 loading strain-rate effects on the material properties (Rafsanjani et al. 2015b). A multi-surface plasticity
121 model, the so-called composite interface model, is typically considered for the mortar joints and is
122 suitable to reproduce fracture, frictional slip and crushing along the interface elements.

123 The assumption that all the inelastic phenomena occur in the interface elements leads to a robust type
124 of modeling, which can follow the complete load path of a structure until the total degradation of
125 stiffness. For a 3D configuration, the linear elastic relation between the generalized stresses and strains
126 of the interface FE is given by $\boldsymbol{\sigma} = \mathbf{D}\boldsymbol{\varepsilon}$, whereas the stiffness matrix is $\mathbf{D} = \text{diag}\{k_n, k_s, k_t\}$ (the
127 subscript n refers to the normal and the subscripts s and t to the shear components).

128 The constitutive interface model is defined by a convex composite yield criterion with three individual
 129 functions, specifically: (i) a tension cut-off criterion designated as $f_{criterion,1}$ and defined in Eq. (1);
 130 (ii) a Mohr-Coulomb shear criterion designated as $f_{criterion,2}$ and defined in Eq. (2); and (iii) a cap in
 131 compression designated as $f_{criterion,3}$ and defined in Eq. (3). Softening behavior is represented in all
 132 the modes. The tensile criterion (Fig. 2a) reads:

$$133 \quad f_{criterion,1}(\boldsymbol{\sigma}, \kappa_1) = \sigma - \bar{\sigma}_1(\kappa_1) \quad \text{and} \quad \bar{\sigma}_1 = f_t \exp\left(-\frac{f_t}{G_f^I} \kappa_1\right) \quad (1)$$

134 The shear criterion (Fig. 2b) is given as:

$$135 \quad f_{criterion,2}(\boldsymbol{\sigma}, \kappa_2) = |\tau| + \sigma \tan\phi(\kappa_2) - \bar{\sigma}_s(\kappa_2) \quad \text{and} \quad \bar{\sigma}_2 = c \exp\left(-\frac{c}{G_f^{II}} \kappa_2\right) \quad (2)$$

136 For the compressive yield function (Fig. 2c) and using a matrix form:

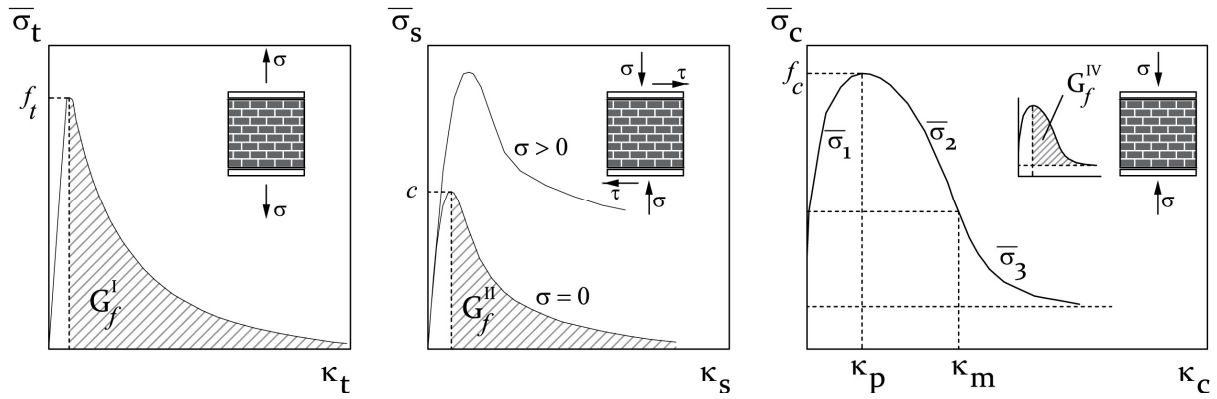
$$137 \quad f_{criterion,3}(\boldsymbol{\sigma}, \kappa_3) = 1/2 (\boldsymbol{\sigma}^T \mathbf{P} \boldsymbol{\sigma}) + \mathbf{p}^T \boldsymbol{\sigma} - \bar{\sigma}_3^2(\kappa_3) \quad (3)$$

138 Here, $\boldsymbol{\sigma}$ is the generalized stresses, f_t is the interface bond strength, c is the interface cohesion strength,
 139 ϕ is the friction angle; \mathbf{P} is a projection diagonal matrix and \mathbf{p} a projection vector based on material
 140 parameters; G_f^I, G_f^{II} are the mode-I and mode-II fracture energy terms, respectively; $\bar{\sigma}_1, \bar{\sigma}_2$ and $\bar{\sigma}_3$ are
 141 the effective stresses of each the adopted yield functions governed by the internal scalar variables κ_1, κ_2
 142 and κ_3 , respectively. Note that the typical compressive hardening/softening law $\bar{\sigma}_3(\kappa_3)$ is composed of
 143 three branches, as observed in Fig. 2c, which are in agreement with the $\bar{\sigma}_{c1}(\kappa_3), \bar{\sigma}_{c2}(\kappa_3)$ and $\bar{\sigma}_{c3}(\kappa_3)$
 144 laws defined in (Paulo B. Lourenço and Rots 1997) and presented in Eq. (4). Note that the subscripts
 145 i, m and r for both the yield stress value and scalar κ indicates the initial, medium and residual values,
 146 respectively. The compressive fracture energy G_f^{IV} depicted in Fig. 2c corresponds to a material input
 147 parameter of the model and allows computing the residual strength value $\bar{\sigma}_r$ (from the peak $\bar{\sigma}_p$ one).

$$148 \quad \bar{\sigma}_{c1}(\kappa_3) = \bar{\sigma}_i + (\bar{\sigma}_p - \bar{\sigma}_i) \sqrt{\frac{2\kappa_3 - \kappa_3^2}{\kappa_p} - \frac{\kappa_3^2}{\kappa_p^2}} \quad (4a)$$

$$149 \quad \bar{\sigma}_{c2}(\kappa_3) = \bar{\sigma}_p + (\bar{\sigma}_m - \bar{\sigma}_p) \left(\frac{\kappa_3 - \kappa_p}{\kappa_m - \kappa_p}\right)^2 \quad (4b)$$

$$150 \quad \bar{\sigma}_{c3}(\kappa_3) = \bar{\sigma}_r + (\bar{\sigma}_m - \bar{\sigma}_p) \exp\left(m \frac{\kappa_3 - \kappa_m}{\bar{\sigma}_m - \bar{\sigma}_r}\right)^2, \quad m = 2 \frac{\bar{\sigma}_m - \bar{\sigma}_p}{\kappa_m - \kappa_p} \quad (4c)$$



151
 152 Fig. 2 – Multi-surface plasticity model adopted for the mortar joints (interface FEs). The behavior of
 153 quasi-brittle materials under (a) tensile loading (mode-I, f_t is the tensile strength); (b) shear loading
 154 (mode-II, c is the cohesion) accounting with a potential pre-compression level; and (c) compressive
 155 load (f_c is the compressive strength; p and m are the peak and medium values, respectively).

156 It may be highlighted that a penalty approach is not followed by the adopted interface FEs to
 157 phenomenologically represent the behavior of masonry crushing. Here, penetration and overlapping
 158 between neighboring brick units can occur which does not blur the adequacy of the strategy. The
 159 dynamic interface model has been implemented in the software DIANA (2017) (strain-rate
 160 independent) and in ABAQUS (2013) (strain-rate dependent). In the latter, a FORTRAN user-
 161 subroutine was developed, and the material model is introduced by a failure criterion. A Euler backward
 162 algorithm (linear predictor-plastic corrector approach) is adopted for the stress update process. The user-
 163 subroutine VUINTER provided in ABAQUS is involved to define contact interface behavior. The
 164 interface material is assumed to be bonded to each of two contacting surfaces (slave and master
 165 surfaces) and, again, the material strength values are sensitive to the load strain-rate level (see (Lourenço
 166 and Rots 1997; Rafsanjani et al. 2015b) for further details).

167 3.2 FE macroscopic model

168 Several continuum models have been presented in the literature albeit especially indicated for concrete-
 169 like materials, such as the well-known ‘Barcelona’ model by (Lubliner et al. 1989), the ‘Microplane’
 170 model by (Bažant et al. 1996), the Concrete Damage Plasticity (CDP) model by (Lee and Fenves 1998),
 171 and the Pontiroli, Rouquard, and Mazars (PRM) model presented in (Pontiroli et al. 2010). Here, a
 172 plasticity continuum model is presented for the static and dynamic study of masonry. The model stems

173 from the anisotropic continuum model for masonry shells and plates proposed in (Lourenço 1997,
 174 2000), in which the so-called composite yield criterion is defined. The formulation is briefly recalled
 175 here for a 3D stress space, whereas the stress and strain tensors are typically represented as six-
 176 components vectors owing the symmetry conditions, and given as follows:

$$177 \quad \boldsymbol{\sigma} = \{\sigma_x, \sigma_y, \sigma_z, \tau_{xy}, \tau_{yz}, \tau_{xz}\}^T$$

$$178 \quad \boldsymbol{\varepsilon} = \{\varepsilon_x, \varepsilon_y, \varepsilon_z, \gamma_{xy}, \gamma_{yz}, \gamma_{xz}\}^T$$

179 The anisotropy of the material behavior is considered since different hardening /softening regimes can
 180 be introduced for different axes. The so-called composite yield surface from (Lourenço 1997) is adopted
 181 and, therefore, a total of three Rankine-type yield criterion are defined in tension and a Hill-type
 182 criterion in compression.

183 *Tension: a Rankine-type criterion*

184 An adequate formulation of the Rankine criterion reads as a single function governed by the first
 185 principal stress and one yield value $\bar{\sigma}_t$ that rules the hardening/softening of the material:

$$186 \quad f_1 = \frac{\sigma_x + \sigma_y}{2} + \sqrt{\left(\frac{\sigma_x - \sigma_y}{2}\right)^2 + \tau_{xy}^2} - \bar{\sigma}_t(\kappa_t) \quad (5)$$

187 where κ_t is the scalar that governs the amount of hardening/softening. Considering the three symmetric
 188 planes xy , yz and xz , designated as $i=1,2$ and 3 respectively, one can write Eq. (5) in a matrix form:

$$189 \quad f_i = \left(\frac{1}{2} \boldsymbol{\xi}_i^T \mathbf{P}_{t,i} \boldsymbol{\xi}_i\right)^{1/2} + \frac{1}{2} \boldsymbol{\pi}_i^T \boldsymbol{\xi}_i \quad (6)$$

189 Here, $\boldsymbol{\xi}_i$ is the reduced stress vector given by $\boldsymbol{\xi}_i = \boldsymbol{\sigma} - \boldsymbol{\eta}_i$. The stress vector $\boldsymbol{\sigma}$ represents the six-
 190 components of the stress field and reads as $\boldsymbol{\sigma} = \{\sigma_x, \sigma_y, \sigma_z, \tau_{xy}, \tau_{yz}, \tau_{xz}\}^T$; the back stress vector $\boldsymbol{\eta}_i$ is
 191 given as $\boldsymbol{\eta}_1 = \{\bar{\sigma}_{tx}(\kappa_{t,1}), \bar{\sigma}_{ty}(\kappa_{t,1}), 0, 0, 0, 0\}^T$ for the xy -plane, as $\boldsymbol{\eta}_2 = \{0, \bar{\sigma}_{ty}(\kappa_{t,2}), \bar{\sigma}_{tz}(\kappa_{t,2}), 0, 0, 0\}^T$
 192 for the yz -plane, and $\boldsymbol{\eta}_3 = \{\bar{\sigma}_{tx}(\kappa_{t,3}), 0, \bar{\sigma}_{tz}(\kappa_{t,3}), 0, 0, 0\}^T$ for the xz -plane. Likewise, the projection
 193 vector reads $\boldsymbol{\pi}_1 = \{1, 1, 0, 0, 0, 0\}^T$, $\boldsymbol{\pi}_2 = \{0, 1, 1, 0, 0, 0\}^T$ and $\boldsymbol{\pi}_3 = \{1, 0, 1, 0, 0, 0\}^T$. The projection matrix
 194 $\mathbf{P}_{t,i}$ is defined for each of the indexes $1, 2, 3$ as:

$$\begin{aligned}
196 \quad \mathbf{P}_{t,1} &= \begin{bmatrix} 1/2 & -1/2 & 0 & 0 & 0 & 0 \\ & 1/2 & 0 & 0 & 0 & 0 \\ & & 0 & 0 & 0 & 0 \\ & & & 2\alpha_1 & 0 & 0 \\ & sym & & & 0 & 0 \\ & & & & & 0 \end{bmatrix} \\
197 \quad \mathbf{P}_{t,2} &= \begin{bmatrix} 0 & 0 & 0 & 0 & 0 & 0 \\ & 1/2 & -1/2 & 0 & 0 & 0 \\ & & 1/2 & 0 & 0 & 0 \\ & & & 0 & 0 & 0 \\ sym & & & & 2\alpha_2 & 0 \\ & & & & & 0 \end{bmatrix} \quad (7) \\
198 \quad \mathbf{P}_{t,3} &= \begin{bmatrix} 1/2 & 0 & -1/2 & 0 & 0 & 0 \\ & 0 & 0 & 0 & 0 & 0 \\ & & 1/2 & 0 & 0 & 0 \\ & & & 0 & 0 & 0 \\ & sym & & & 0 & 0 \\ & & & & & 2\alpha_3 \end{bmatrix}
\end{aligned}$$

199 It is important to recall that the yield stress values $\bar{\sigma}_{tx}(\kappa_{t,i})$, $\bar{\sigma}_{ty}(\kappa_{t,i})$, $\bar{\sigma}_{tz}(\kappa_{t,i})$ are described by
200 exponential softening rules:

$$\begin{aligned}
201 \quad \bar{\sigma}_{tx}(\kappa_{t,i}) &= f_{tx} \exp\left(-\frac{hf_{tx}}{G_{f_{tx}}} \kappa_{t,i}\right) \\
202 \quad \bar{\sigma}_{ty}(\kappa_{t,i}) &= f_{ty} \exp\left(-\frac{hf_{ty}}{G_{f_{ty}}} \kappa_{t,i}\right) \quad (8) \\
203 \quad \bar{\sigma}_{tz}(\kappa_{t,i}) &= f_{tz} \exp\left(-\frac{hf_{tz}}{G_{f_{tz}}} \kappa_{t,i}\right)
\end{aligned}$$

204 where f_{tx} , f_{ty} , f_{tz} are the material uniaxial tensile strength values and $G_{f_{tx}}$, $G_{f_{ty}}$, $G_{f_{tz}}$ the material
205 tensile fracture energies according to the material axes; and h is the equivalent length related to the
206 finite element size according to (Bažant and Oh 1983) aiming the fracture energy regularization. A non-
207 associated plastic potential g_i has been considered and reads as:

$$208 \quad g_i = \left(\frac{1}{2} \xi_i^T \mathbf{P}_{g,i} \xi_i\right)^{1/2} + \frac{1}{2} \boldsymbol{\pi}_i^T \xi_i \quad (9)$$

209 where $\mathbf{P}_{g,i}$ is the projection matrix that represents the Rankine plastic flow, given by (7) for an
210 $\alpha_1, \alpha_2, \alpha_3 = 1$. The inelastic behavior is ruled by a strain-softening hypothesis, in which the scalar in
211 rate form $\dot{\kappa}_{t,i}$ is written in terms of the plastic multiplier rate $\dot{\lambda}_{t,i}$, i.e. $\dot{\kappa}_{t,i} = \dot{\lambda}_{t,i}$.

212 *Compression: A Hill-type criterion*

213 A Hill-type criterion is used to characterize the yield condition of masonry in compression assuming a
 214 rotated centered ellipsoid shape. The formulation is considered in the 3D stress space for convenience
 215 and includes different compressive strength values along the different material axes. In a matrix form,
 216 the yield criterion can be written as:

$$219 \quad f_4 = \left(\frac{1}{2} \boldsymbol{\sigma}^T \mathbf{P}_c \boldsymbol{\sigma} \right)^{1/3} - \bar{\sigma}_c(\kappa_c) \quad (10)$$

217 where $\bar{\sigma}_c$ is the yield value along the three material axes given by $\bar{\sigma}_c(\kappa_c) = \sqrt[3]{\bar{\sigma}_{cx}(\kappa_c)\bar{\sigma}_{cy}(\kappa_c)\bar{\sigma}_{cz}(\kappa_c)}$.

218 The projection matrix \mathbf{P}_c is computed through Eq. (11):

$$220 \quad \mathbf{P}_c = \begin{bmatrix} 2 \frac{\bar{\sigma}_{cy}\bar{\sigma}_{cz}}{\bar{\sigma}_{cx}^2} & \beta_1 & \beta_2 & 0 & 0 & 0 \\ & 2 \frac{\bar{\sigma}_{cx}\bar{\sigma}_{cz}}{\bar{\sigma}_{cy}^2} & 0 & 0 & 0 & 0 \\ & & 2 \frac{\bar{\sigma}_{cx}\bar{\sigma}_{cy}}{\bar{\sigma}_{cz}^2} & 0 & 0 & 0 \\ & & & 2\gamma_1 & 0 & 0 \\ & sym & & & 2\gamma_2 & 0 \\ & & & & & 2\gamma_3 \end{bmatrix} \quad (11)$$

221 The parameters β_1, β_2 and $\gamma_1, \gamma_2, \gamma_3$ influence the shape of the yield criterion. The parameters β_i
 222 controls the coupling between the normal stress values and should be obtained experimentally (P.B.

223 Lourenço 1997), and the parameters γ_i are obtained as $\gamma_1 = \frac{(f_{cx}f_{cy})}{\tau_{u,c}^2}, \gamma_2 = \frac{(f_{cy}f_{cz})}{\tau_{u,c}^2}$ and $\gamma_3 =$

224 $\frac{(f_{cx}f_{cz})}{\tau_{u,c}^2}$. Here, f_{cx}, f_{cy}, f_{cz} are the uniaxial compressive strengths in the x-, y- and z- directions

225 respectively and $\tau_{u,c}$ the fictitious material pure shear strength in compression. The inelastic law of the
 226 material in the compressive regime comprehend a parabolic hardening followed by a
 227 parabolic/exponential softening, whereas different fracture energy values may be defined according to
 228 the material axes, i.e. G_{fcx}, G_{fcy} and G_{fcz} .

229 The anisotropic macro-model has been implemented in the advanced software DIANA (2017) (strain-
 230 rate independent) and in ABAQUS (2013). In the latter, a FORTRAN user-subroutine VUMAT was
 231 developed, in which the material model and the procedure to update the stress vector and state variables
 232 has been provided.

233 3.3 A simplified multi-scale (FE²) homogenization-based model

234 A simplified two-step numerical procedure has been recently introduced by the authors in (Silva, et al.
235 2017a, 2017b). The aim has been the prediction of the static and dynamic mechanical response of
236 periodic masonry structures, whereas both the masonry orthotropy and material nonlinear behavior can
237 be represented under an attractive computational burden. The strategy makes use of a classical first-
238 order homogenization scheme and is formed by three steps: (i) the definition and solution of the meso-
239 scale problem; (ii) the implementation of the meso-to-macro transition; and (iii) the solution of the
240 macro-scale problem.

241 *Meso-scale (FE-based mesoscopic model)*

242 A unit-cell homogenization approach is employed at a meso-scale. The strategy can be designated as
243 an up-ward procedure, i.e. information regarding the mechanical characterization at a cell level is
244 transferred into the macro-scale. Different numerical models can be employed at a meso-scale and,
245 therefore, the accuracy of the strategy is highly dependent on the accuracy of the latter. It relies on a
246 micro-modeling approach and involves solving a mechanical problem on a representative volume
247 element (RVE) to derive average field variables. The authors have employed a Kirchhoff-Love (KP)
248 and a Mindlin-Reissner (MP) plate FE models but it is possible to use a three-dimensional model (3D
249 DNS), see (Silva et al. 2018) for further details. The units are elastic and the material nonlinearity is
250 assumed to be lumped in the joints aiming at the decrease of the computational effort. This assumption
251 seems to be specially adequate for strong block masonry structures (Sinha 1978; Herbert et al. 2014).
252 Units are modeled as quadrilateral FEs and mortar joints through zero-thickness interface FEs. The
253 multi-surface plasticity model presented in section 3.1 has been considered for the interface elements.
254 The RVE needs to be statistically representative of the macro-scale level (Hill 1965) and sufficiently
255 small to respect the principle of scales separation of first-order homogenization theory. Since a
256 bespoke model for periodic masonries has been proposed (Silva et al. 2018), the recommendations by
257 Anthoine (1995) are followed for the definition of the RVE within a running-bond and English-bond
258 masonries. Accordingly, a rectangular pattern with more than one brick unit and within a rectangular
259 basic cell is defined to represent the RVE of study, as seen in the next section. The RVE is herein
260 denoted as Ω_m . The kinematical description of the homogenization-based models for the in-plane case

261 relies on the assumption that the macroscopic strain tensor \mathbf{E} is obtained as the volume average of the
 262 mesoscopic strain field $\boldsymbol{\varepsilon}_m = \boldsymbol{\varepsilon}_m(\mathbf{y})$ at each point over the associated RVE:

$$263 \quad \mathbf{E} = \frac{1}{V_m} \int_{\Omega_m} \boldsymbol{\varepsilon}_m dV \quad (12)$$

264 where V_m is the volume of the RVE. The mesoscopic strain field can be decomposed into a macro-scale
 265 and meso-scale contribution. The latter is referred to as an additive decomposition of the mesoscopic
 266 strain tensor $\delta\boldsymbol{\varepsilon}_m = \delta\boldsymbol{\varepsilon}_m(\mathbf{y})$, and given as $\delta\boldsymbol{\varepsilon}_m = \delta\mathbf{E} + \nabla^s u_m$, where $\delta\mathbf{E}$ is the applied constant strain
 267 tensor over the RVE and $\nabla^s u_m$ is the gradient of the fluctuation displacement field. Considering that $\boldsymbol{\sigma}_m$
 268 is the mesoscopic stress field, upon RVE equilibrium, the homogenized generalized stresses can be
 269 derived. The Hill-Mandell principle is based on an energetic equivalence between the macroscopic and
 270 mesoscopic work, as follows:

$$271 \quad \boldsymbol{\Sigma} : \delta\mathbf{E} = \frac{1}{V_m} \int_{\Omega_m} \boldsymbol{\sigma}_m : \delta\boldsymbol{\varepsilon}_m d\Omega \quad (13)$$

272 in which $\boldsymbol{\Sigma}$ is the macroscopic stress tensor. According to the assumed additive decomposition of the
 273 mesoscopic strain tensor, one may obtain the macro-homogeneity principle as:

$$274 \quad \boldsymbol{\Sigma} : \delta\mathbf{E} = \frac{1}{V_m} \int_{\Omega_m} \boldsymbol{\sigma}_m : \delta\mathbf{E} d\Omega + \frac{1}{V_m} \int_{\Omega_m} \boldsymbol{\sigma}_m : \nabla^s \delta u_m d\Omega \quad (14)$$

275 for any kinematical admissible δu_m . Periodic boundary conditions are assumed to solve the boundary
 276 value problem. Such consideration is extensively found in homogenization procedures (Blanco et al.
 277 2016) also for the particular case of masonry structures (Cecchi and Sab 2002b; Milani et al. 2006a;
 278 Otero et al. 2015). The periodic boundary conditions lead to a kinematical field that enforces anti-
 279 periodicity of the tractions to occur. Due to the periodicity of the displacement fluctuations on the
 280 boundaries, the Eq. (14) can be simplified and expressed as:

$$281 \quad \boldsymbol{\Sigma} : \delta\mathbf{E} = \frac{1}{V_m} \int_{\Omega_m} \boldsymbol{\sigma}_m : \delta\mathbf{E} d\Omega, \quad \forall \delta\boldsymbol{\varepsilon} \quad (15)$$

282 Thus, the corollary of the Hill-Mandell principle is that the homogeneous macroscopic stress tensor Σ
 283 can be written as the volume average of the mesoscopic stress field $\sigma_m = \sigma_m(y)$ over the RVE:

$$284 \quad \Sigma = \frac{1}{V_m} \int_{\Omega_m} \sigma_m d\Omega \quad (16)$$

285 The variational principle and the use of periodic boundary conditions allow concluding that the external
 286 surface tractions and body force field on the RVE are reactive terms over the imposed kinematical
 287 conditions. These kinematical boundary conditions are dependent on the deformation modes considered
 288 at the meso-mechanical level. Thus, the in-plane static equilibrium of the RVE is reached, for each
 289 kinematic constraint considered, without any external surface traction and body force terms. The
 290 variational principle holds when accounting for the out-of-plane quantities to assure the energy
 291 consistency between scales. The difference lies in the replacement of generalized stresses through
 292 moment and force terms.

293 The homogenization technique is followed and, by solving the internal static RVE equilibrium using a
 294 classical FE-procedure, the homogenized Σ and \mathbf{E} quantities are derived. Furthermore, the macro-stress
 295 couples are obtained by through-the-thickness integration of the homogeneous macro-stresses
 296 according to Eq. (17); wherein i,j refers to the index x or y (M_{xx}, M_{xy}, M_{yy}). The numerical integration
 297 is performed accounting only the mid-plane reference surface ω . The obtained homogenized moment-
 298 curvature relations are defined per unit of length.

$$299 \quad M_{ij} = \int_{-z/2}^{z/2} \sigma_{m,ii} z dz \quad (17)$$

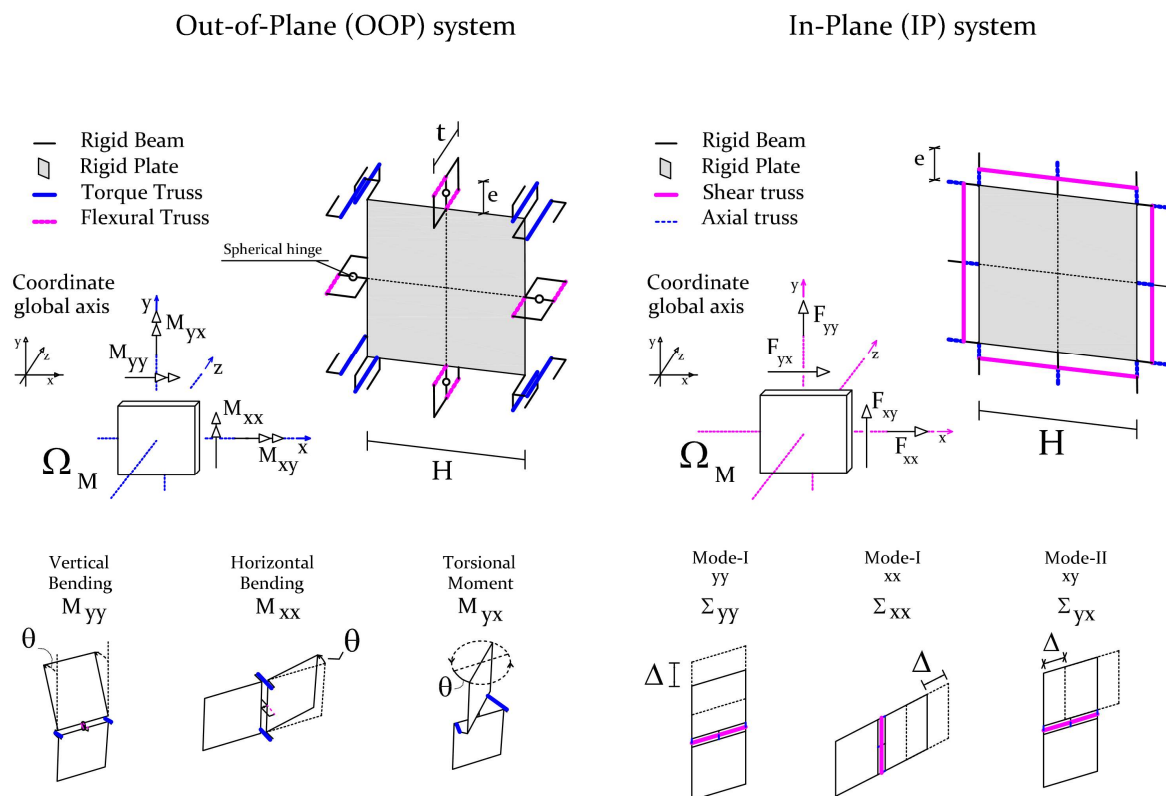
300 *Macro-scale (FE discrete model)*

301 Discrete FE-method based strategies, designated in the literature as rigid body spring models (RBSMs),
 302 represent masonry as the assembly of rigid blocks interconnected by discrete interfaces whereas the
 303 deformation is represented through normal and tangential springs. RBSMs are supported in the
 304 theoretical background of Kawai (1978) works. Yet, some differences exist between RBSMs and other
 305 discrete-based strategies, as the discrete (or distinct) element method (DEM) or the applied element

306 method (AEM). In fact, FE methods may not be so efficient for problems in which several discontinuous
307 exists in the media leading to a situation where several distinct bodies exhibit large relative movements.
308 In such problems, where the contact conditions vary during the analysis and large displacements are
309 expected, using the DEM strategy for the masonry modeling seems the best choice, see (Cundall and
310 Hart 1971; Lemos 2007). DEM is, however, based on explicit numerical procedures and its usage within
311 a dynamic analysis of masonry structures can be prohibitive due to the involved computational
312 processing times. Concerning the AEM, firstly proposed by (Meguro and Tagel-Din 2000), it has
313 analogous features with the RBSMs. It represents masonry through the assembly of rigid elements
314 interconnected by discrete interfaces that are also modeled through normal and shear non-linear springs.
315 The main differences between AEM and RBSM lie on the fact that the former assumes recontact
316 between neighboring discrete elements after the occurrence of collapse and that it tends to employ a
317 micro-modeling approach to describe masonry (Guragain et al. 2006; Malomo et al. 2018). The latter
318 can be a contentious issue when engineering larger structures. In converse, RBSMs allow to adopt
319 coarser scales meshes within a macro-modeling approach for masonry and, therefore, increase the
320 computational efficiency.

321 Several RBSMs are found in the literature, as the one implemented by (Caliò et al. 2012) for the in-
322 plane study of masonry and extended to the out-of-plane application by (Pantò et al. 2017); and the
323 work of (Casolo 1999) whereas the out-of-plane behavior of a masonry façade was investigated. The
324 latter RBSM strategies are quite promising from a computational standpoint but demand the calibration
325 of both the material and mechanical properties assigned to the nonlinear springs. Such a procedure can
326 lead to loss of the physical meaning of the input parameters and may be arguable in cases where
327 experimental evidence is lacking. Hence some authors coupled different RBSMs within two-scale
328 strategies, wherein the material information of the springs is computed through homogenization
329 strategies. For instance, Milani et al. (2006) implemented a limit analysis-based two-scale strategy in
330 which an RBSM, represented through rigid triangular constant stress elements and rotational interface
331 springs, is linked with a simple homogenization strategy for the study of URM panels. Similarly, Casolo
332 and Milani (2010) and Casolo and Uva (2013) adopted, respectively, a homogenization-based RBSM
333 using quadrilateral rigid elements and rotational interface springs for the nonlinear static and dynamic

334 analysis of masonry structures, respectively. The existing strategies typically focus on the out-of-plane
 335 behavior only and in the use of simplified analysis methods at a macro-scale, as limit-analysis, to
 336 improve the strategies robustness in the presence of material softening for quasi-static problems.
 337 In such a context, a discrete FE-method based procedure is proposed and implemented into the advanced
 338 finite element software ABAQUS (2013). It stems from the RBSM model presented in (Silva et al.
 339 2017a, 2017b) which is suitable only for the out-of-plane analysis of masonry structures. Thus, an
 340 improved and innovative RBSM is here addressed as it incorporates both the in- and out-of-plane
 341 behavior of masonry being also coupled with the presented novel homogenization strategy.
 342 The RBSM model is composed by the assemblage of discrete quadrilateral rigid plate elements
 343 interconnected, at its interfaces, through a set of rigid and deformable truss FEs, see Fig. 3 (equivalent
 344 to spring elements). The truss elements govern both the deformation and damage of the structure by
 345 being able to mimic the presence of the in- and out-of-plane failure modes considered in Fig. 3 and
 346 within a decoupled characterization. These can append the material information of the meso-scale
 347 homogenized step and thus represent the masonry texture via an equivalent continuum medium.



348
 349 Fig. 3 – Description of the basic in- and out-of-plane FE truss/beam systems of the discrete macro-unit
 350 cell.

351 The two-scale simplified procedure allows processing the meso to macro-scale transition only once and,
352 therefore, achieve low computational times. The main advantages of the procedure are threefold: (1)
353 several strategies with different complexities can be employed at a meso-scale; (2) the concrete damage
354 plasticity (CDP) model implemented in ABAQUS can properly characterize the constitutive material
355 model of the truss elements at a macro-scale, as it suitable to fully reproduce the homogenized response
356 of the masonry RVE; and (3) the computational robustness in presence of material softening can be
357 guaranteed for quasi-static problems by arc-length procedures available in ABAQUS software.
358 Specifically, the model combines a stress-based plasticity with a strain-based scalar damage and can
359 reproduce several macroscopic properties for tension and compression regimes, such as different yield
360 strengths and so represent masonry orthotropy; different stiffness degradation values, and so represent
361 the masonry full softening behavior; different recovery effect terms; and rate sensitivity, which can
362 increase the peak strength value depending on the response strain rate. Moreover, it does consider the
363 latter in the presence of interfaces dynamic and/or cyclic loading and is integrated using the backward
364 Euler method. A general overview of the main features of CDP for the rate-independent model are
365 presented next, being the reader referred to e.g. Lubliner et al. (1989) and Lee and Fenves (1998) for
366 further details.

367 Effective stresses govern the plastic part of these models (Grassl and Jirásek 2006) and the stress-strain
368 relationship is ruled, as referred, by an isotropic damage scalar affecting the elastic stiffness of the
369 material. The nominal stress tensor $\boldsymbol{\sigma}$ reads:

$$370 \quad \boldsymbol{\sigma} = (1 - d)\mathbf{E}_0^{el} : (\boldsymbol{\varepsilon} - \boldsymbol{\varepsilon}^{pl}) = \mathbf{E} : (\boldsymbol{\varepsilon} - \boldsymbol{\varepsilon}^{pl}) \quad (18)$$

371 where \mathbf{E}_0^{el} is the initial elastic stiffness of the material; d is the damage parameter, which defines the
372 stiffness degradation (0 for an undamaged and 1 for a fully damaged material), and is designated as d_t
373 and d_c for tension and compression regimes, respectively; $\boldsymbol{\varepsilon}$ is the total strain tensor; $\boldsymbol{\varepsilon}^{pl}$ is the plastic
374 strain tensor, and \mathbf{E} is the initial elastic stiffness of the material affected by the damage parameters (the
375 degraded initial stiffness given by $\mathbf{E} = (1 - d)\mathbf{E}_0^{el}$).

376 A non-associated flow-rule is assumed for the plasticity model and given by:

$$377 \quad \dot{\boldsymbol{\varepsilon}}^{pl} = \dot{\lambda} \frac{\partial g_p}{\partial \boldsymbol{\sigma}} (\bar{\boldsymbol{\sigma}}, \boldsymbol{\kappa}_p) \quad (19)$$

378 in which $\dot{\boldsymbol{\varepsilon}}^{pl}$ is the rate of the plastic strain, $\dot{\lambda}$ is the rate of the plastic multiplier, g_p is the plastic potential,
 379 $\bar{\boldsymbol{\sigma}}$ is the effective stress tensor, and κ_p the hardening/softening variable. The rate of the
 380 hardening/softening variable $\dot{\kappa}_p$ is related to the rate of plastic strain given by an evolution law \mathbf{h} , as
 381 seen in Eq. (20):

$$382 \quad \dot{\kappa}_p = \mathbf{h}(\bar{\boldsymbol{\sigma}}, \kappa_p) : \dot{\boldsymbol{\varepsilon}}^{pl} \quad (20)$$

383 The CDP model uses a yield function based on the works of Lubliner et al. (1989) and Lee and Fenves
 384 (1998). The hardening parameter that controls the meridians shape of the yield shape is given by $K_c =$
 385 $2/3$, which leads to an approximation of the Mohr-Coulomb criterion.

386 Hence, following the input requirements for the CDP model it is mandatory to obtain effective stress
 387 and strain curves for each angle of the interface and for each bending moment direction. In other words,
 388 the material orthotropy is reproduced at a structural level because the approach offers the possibility to
 389 reproduce different input stress-strain relationships according to the trusses plane. To what concerns the
 390 in-plane behavior, the stress quantities are directly derived from the mesoscopic homogenized values
 391 scaled according to the length of the macro-interfaces. For the out-of-plane behavior, the conversion
 392 from moment to stress values must be achieved following Eq.(21) and Eq.(22):

$$393 \quad \sigma_{Bending\ truss} = \frac{M}{(A_{Bending\ truss} \times e)} \quad (21)$$

$$394 \quad \sigma_{Torsional\ truss} = \frac{M}{(A_{Torsional\ truss} \times H)} \quad (22)$$

395 Here, M is the bending moment per unit of interface length, H the length of each quadrilateral panel (L
 396 is the influence length of each truss and is equal to half of the mesh size, i.e. $H/2$), t is the thickness of
 397 the wall, $A_{Bending\ truss}$ and $A_{Torsional\ truss}$ are the bending and torsional truss areas, respectively, and
 398 are given by $0.5 \times e \times H$ where e (value of 10 mm) is the gap between the rigid plates, which ideally should
 399 be zero but in practice is assumed small enough to be able to place trusses between elements.

400 At last, the stress homogenized input curves may be properly calibrated (so-called regularization). An
 401 elastic calibration for the stress curves is conducted. The latter is guaranteed separately for both in-
 402 plane and out-of-plane modes and, therefore, a decoupled behavior is derived. Briefly, by assuring the
 403 energy equivalence between the discrete mechanism and a homogeneous continuous plate element it

404 can be easily derived that, for both case studies, the Young's moduli of axial, shear, bending and
 405 torsional truss elements is given as:

$$406 \quad E_{ii}^{In-plane \text{ axial truss}} = \frac{\bar{E}_{ii}e}{4L + 2e} ; E_{xy}^{In-plane \text{ shear truss}} = \frac{\bar{G}_{xy}H^2}{4e(2L + e)} \quad (23)$$

$$407 \quad E_{ii}^{Bending \text{ truss}} = \frac{\bar{E}_{ii}t^4H}{12(1 - \nu^2)(H + e)e^3H} ; E^{Torsional \text{ truss}} = \frac{2\bar{G}_{xy}t^4}{3H^2e(2L + e)} \quad (24)$$

408 where \bar{G}_{xy} is the homogenized shear modulus given directly by the slope of the shear meso-scale
 409 homogenized curve; \bar{E}_{ii} is the Young's moduli of the masonry in the direction ii (i represents the
 410 cartesian axis x or y); and ν is the Poisson coefficient for the homogeneous media. After the calibration
 411 and aiming to fulfill the input requirements for the CDP model in ABAQUS, the information regarding
 412 the post-failure behavior may be introduced for each element that features material nonlinearity in terms
 413 of effective stress and inelastic strain $\tilde{\varepsilon}^{ck}$ values, i.e. the truss elements. Since truss elements define the
 414 material behavior of the macro-interfaces, the system will undergo only uniaxial loading conditions.
 415 Hence, for the case of uniaxial loading condition, the inelastic strain value must be obtained for each
 416 point of the post-peak homogenized curve according to Eq. (25):

$$417 \quad \tilde{\varepsilon}^{ck} = \varepsilon - \varepsilon_0^{el} \quad (25)$$

418 where ε_0^{el} is the elastic strain corresponding to the undamaged material and ε is the total axial strain of
 419 the multi-linear stress envelope. If the damage parameter d are introduced, the plasticity model is thus
 420 coupled with a damage description and is suitable for the cyclic behavior description of the material.
 421 Again, for the case of uniaxial loading condition and for a given truss element, the plastic strain values
 422 ε^{pl} are calculated for each point of the input curve through Eq. (26). Since the permanent plastic strains
 423 values ε^{pl} can be just positive or null, the latter can constitute a good checkpoint to foresee if the damage
 424 parameters have been properly computed.

$$425 \quad \varepsilon^{pl} = \varepsilon^{cr} - \frac{d}{(1 - d)} \frac{\sigma^P}{E_0^{el}} \quad (26)$$

426 In continuum FE-based frameworks, in which material nonlinearity and cracking are attributed to
 427 continuum elements (through, for instance, the proposed anisotropic macro-model or other models, as
 428 the smeared crack by (Rots et al. 1985)), the strain localization is a key issue and the regularization of

429 the FE material constitutive law is necessary to achieve mesh objectivity of the results. In related multi-
430 scale continuum, FE approaches, as (Petracca et al. 2016; Cervera and Chiumenti 2006) an alike
431 procedure is implemented. This is typically based on the crack band theory by (Bažant and Oh 1983),
432 whereas the definition of a characteristic length that addresses both scales is required to affect the
433 fracture energy of the material constitutive model.

434 For the present homogenization-based strategy, the mesh objectivity problem resorts only on the
435 correction of the material homogenized data according to the discrete macro-mesh refinement rather
436 than the strain localization issue at both scales. This is so because, at a meso-scale, both the material
437 nonlinearity and cracking are placed on mortar joints that are modeled in a discontinuous (interface
438 elements) way (Borst et al. 2006); and, at a macro-scale, an RBSM is adopted in which material
439 softening and cracking is lumped on individual 2-node linear truss elements (one integration point), for
440 which a characteristic length of 1 is generally given (ABAQUS 2013; DIANA 2017).

441 Thus, the so-called regularization step is here performed aiming to correct the elastic stiffness and post-
442 peak fracture energies of the stress-strain curves that serve as input for the CDP model. The derived
443 meso-scale homogenized curves (per interface unit length) are firstly scaled, according to the macro-
444 interface length H , and secondly affected by a regularization factor f_r depending on if it represents an
445 in-plane (normal and shear) or an out-of-plane (flexural and torsional) mode.

446 Consider, for instance, that $\tilde{\mathbf{\epsilon}} = [\epsilon_1 \quad \epsilon_2 \quad \dots \quad \epsilon_{n-1} \quad \epsilon_n]$ and $\tilde{\mathbf{\sigma}} = [\sigma_1 \quad \sigma_2 \quad \dots \quad \sigma_{n-1} \quad \sigma_n]$ are the n -
447 dimensional vectors which define, respectively, the σ - ϵ homogenized curve being regularized (n is the
448 number of points of the curve). After scaling the stress values of $\tilde{\mathbf{\sigma}}$ according to the macro-scale mesh
449 size, it is required to regularize the strain values of $\tilde{\mathbf{\epsilon}}$. In this regard, the regularization factor f_r , is, for
450 a given truss element set, defined as the relation between the elastic stiffness of the σ - ϵ curve under
451 study and the calibrated Young modulus obtained for each deformable truss through Eq.(23)-(24). The
452 procedure to compute the reference elastic stiffness value is assumed to be performed for the designated
453 point C ; the point of the σ - ϵ homogenized curve that has a stress given as one-third of the peak value.
454 Thus, f_r is computed as $f_r = \sigma_C / (\epsilon_C E_{calibrated})$ where, $E_{calibrated}$ is the corrected Young modulus
455 obtained for each truss type following Eq. (23) and Eq. (24).

456 In other words, the regularization terms can be simply written as $f_r^{mode-I} = \bar{E}_{ii,C}/E_{ii}^{in-plane\ axial\ truss}$
457 and $f_r^{mode-II} = \bar{G}_{xy,C}/E_{xy}^{in-plane\ shear\ truss}$ for the in-plane macro-trusses; and as $f_r^{bending} =$
458 $\bar{E}_{ii,C}/E_{ii}^{bending\ truss}$ or $f_r^{torsion} = \bar{G}_{xy,C}/E^{torsional\ truss}$ for the out-of-plane macro-trusses. Such
459 parameters f_r affects all the strains of the homogeneous stress-strain curves of the corresponding
460 trusses. By correcting the strain axis to calibrate the elastic stiffness value the operator affects, as well,
461 the post-peak curve strains and so, in an implicit way, the fracture energy itself. It may be pointed out
462 that, for the out-of-plane truss elements (both the torsion and bending elements), the scaling and the
463 regularization steps are performed only after the conversion of homogenized moment values into stress
464 quantities according to Eq.(21) and Eq.(22).

465 **3.4 Strain-rate dependency of the modeling strategies**

466 The use of static strength properties can lead to inaccurate results when evaluating the masonry behavior
467 under fast dynamic actions since these properties exhibit an enhancement according to the strain rate
468 level of the applied load. Research mainly centered on concrete-like materials can be found in the
469 literature, where assumptions intrinsically related with material effects are reported to explain the
470 phenomena, such as the lateral inertial confinement, end support friction and scale-effect (Hao et al.
471 2013; Y. Hao and Hao 2013; Le Nard and Bailly 2000).

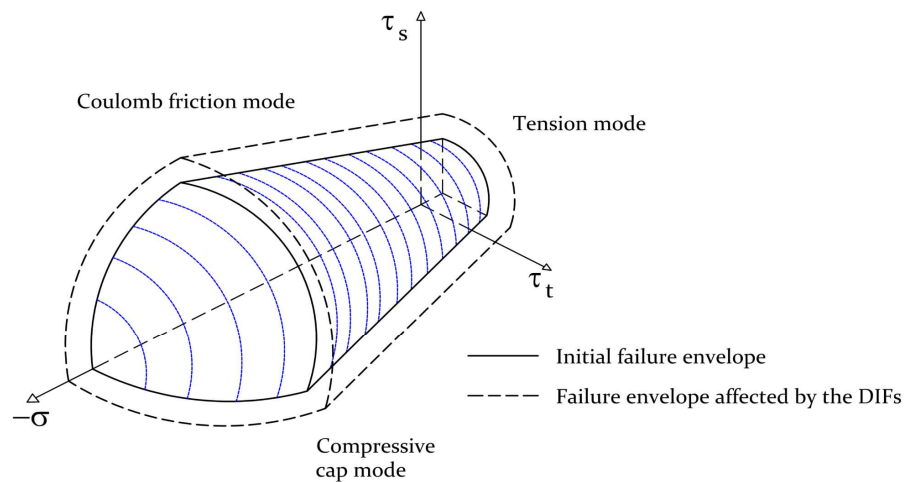
472 Experimentation is, in the field of fast dynamics, still at a higher level with respect to numerical
473 modeling (Buchan and Chen 2007). Some laboratory tests have been performed to evaluate the response
474 of the masonry under such extreme loads, see for (Pereira and Lourenço 2016b; Pereira et al. 2015;
475 Pereira and Lourenço 2016a; Hao and Tarasov 2008; Dennis et al. 2002; Baylot et al. 2005). In converse,
476 few numerical studies on the response of masonry under blast or impact actions are found in the
477 literature; one may recall the contributions by (Wu et al. 2005; Zapata and Weggel 2008; Macorini and
478 Izzuddin 2014; Burnett et al. 2007).

479 The strain-rate dependency of the masonry can be represented through the use of visco-elastic models
480 aiming at strain-rate regularization, as seen in (Sluys and De Borst 1992; Georgin and Reynouard 2003).
481 This seems an adequate and numerically convenient strategy, especially if one notices that introducing,
482 for instance, the well-known Duvaut and Lions (1976) model within an FE plasticity model is well

483 documented. Yet, the definition of a viscosity regularization parameter still lacks objectivity and
484 requires extensive sensitivity studies for the case of masonry.

485 In such a context, the presented inviscid advanced FE formulations have been formulated to account
486 for this phenomenological feature of masonry by making use of dynamic increase factors (DIFs). The
487 authors believe that these numerical models may strongly contribute to further advances on this complex
488 topic. The DIFs directly affect the static material properties adopted and can be introduced in the
489 strategies via: (i) a strain-rate law, typically a logarithmic curve, for each selected parameter; or (ii) a
490 discrete DIF value, independent from the strain rate level, which is a priori assumed and adopted as
491 constant. The former may yield more realistic values, but the latter is straightforward, simple and more
492 aligned with normative proposals. These data can be deduced through experimental campaigns as seen
493 in (Pereira and Lourenço 2016a) and (Hao and Tarasov 2008).

494 According to the information at disposal, different DIF values are obtained for each mechanical
495 parameter of masonry, which allows the expansion or contraction of the strength envelope thus
496 depending on the load strain-rate; as schematically described in Fig. 4 for the case of the composite
497 interface model.



498
499 Fig. 4 – Schematic representation of the yield envelope for the composite interface model adopted
500 affected by the DIFs.

501 4 Applications

502 4.1 Engineering a meso-scale mechanical problem

503 The majority of the existing research on periodic masonry deal with running-bond texture within the
504 case of a single-wythe wall (Milani 2008; Zucchini and Lourenço 2002; Taliervo 2014; Pau and
505 Trovalusci 2012; Reccia et al. 2018). Some features seem still somehow under-investigated, as: (i) the
506 analysis of the effect of potential discontinuities in the masonry thickness, when two- or three-wythes
507 of masonry are present; (ii) the effect of three-dimensional shear stresses; and (iii) the study of other
508 periodic textures, as the English-bond.

509 In this context, a study at a meso-scale is presented next. This is aimed to assess the mechanical effect
510 of the mid-thickness vertical joint of English-bond masonry walls and the effect that three-dimensional
511 shear stresses play. The conclusions are drawn in terms of moment-curvature curves.

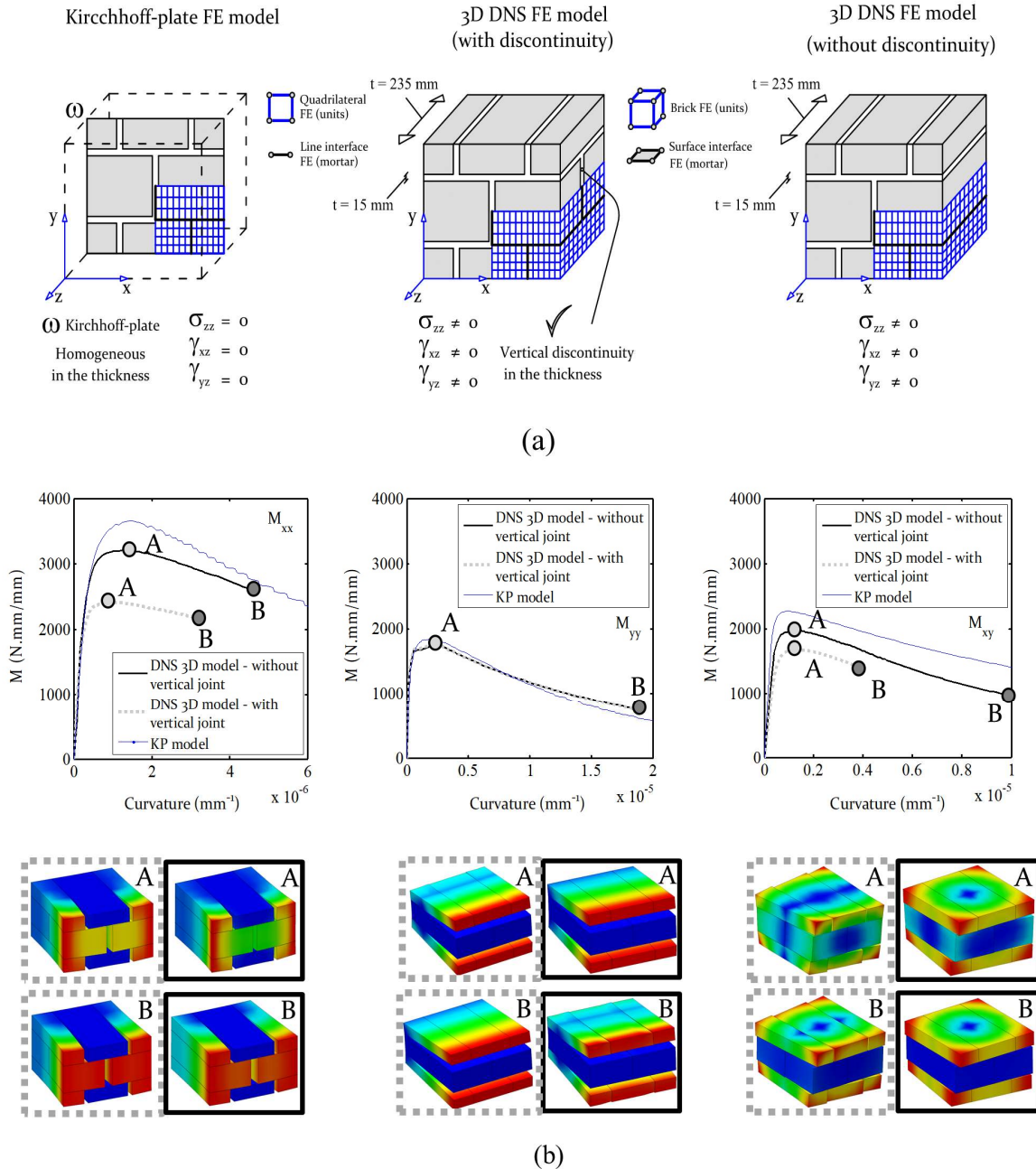
512 The selected case study concerns the English-bond masonry tested experimentally by Candeias et al.
513 (2017). The problem is schematically described in Fig. 5a and three unit-cell models are accounted for.

514 The first-unit cell model advents from a Kirchhoff-plate mesoscopic model in which the aforementioned
515 homogenization scheme (see 3.3) is followed. The remaining two unit-cell models follow a direct
516 numerical simulation (DNS models) or a micro-modeling approach (as referred in 3.1): the latter does
517 not take into account the discontinuity along with the thickness, whereas the former considers it,
518 meaning that it is explicitly modeled. The adopted material properties for units are $E_u = 11,000 \text{ MPa}$;

519 $\nu_u = 0.25$ and for mortar joints $E_m = 2,200 \text{ MPa}$; $\nu_m = 0.20$; and the inelastic mechanical parameters
520 for mortar joint interfaces are given by: $f_t = 0.105 \text{ MPa}$, $G_f^I = 0.012 \text{ N/mm}$, $c = 0.20 \text{ MPa}$, $G_f^{II} =$
521 0.05 N/mm , $\phi = 30 \text{ degrees}$, $f_c = 2.84 \text{ MPa}$; $G_f^{IV} = 4.00 \text{ N/mm}$. For all the cases, the material

522 nonlinearity is lumped in the mortar joints by using interface FEs within the presented multi-surface
523 plasticity model. Note that the linear elastic relation between the generalized stresses and strains of the
524 interface FEs is given by the classical constitutive equation of Hooke's law, $\boldsymbol{\sigma} = \mathbf{D}\boldsymbol{\varepsilon}$. Considering a line
525 FE interface (for the adopted plate theories Kirchhoff-Love (KP) and a Mindlin-Reissner (MP) models),
526 the elastic stiffness matrix \mathbf{D} is given as $\mathbf{D} = \text{diag}\{k_n, k_s\}$. The values of the normal (k_n) and shear (k_s)
527 mortar joints stiffness terms can be easily computed through Eq. (27)-(28), if considered that the

528 masonry components are represented by a serial chain of springs, under a stack-bond, with uniform
 529 stress distributions in both the unit and mortar joints. Therefore, the obtained values for $k_n =$
 530 183 N/mm ; $k_s = 72.6 \text{ N/mm}$, respectively.



531
 532 Fig. 5 – Meso-scale mechanical study of an English-bond masonry texture: (a) numerical models
 533 assumed for the RVE description; (b) results obtained in terms of moment vs. curvature curves using a
 534 KP model and two DNS 3D models: one that considers, and the other that excludes the existent vertical
 535 joint on the mid-thickness. Deformed configurations at peak and ultimate post-peak point are plotted
 536 for both models.

537
$$k_n = \frac{E_u E_m}{t_m (E_u - E_m)} \quad (27)$$

538
$$k_s = \frac{G_u G_m}{t_m (G_u - G_m)} \quad (28)$$

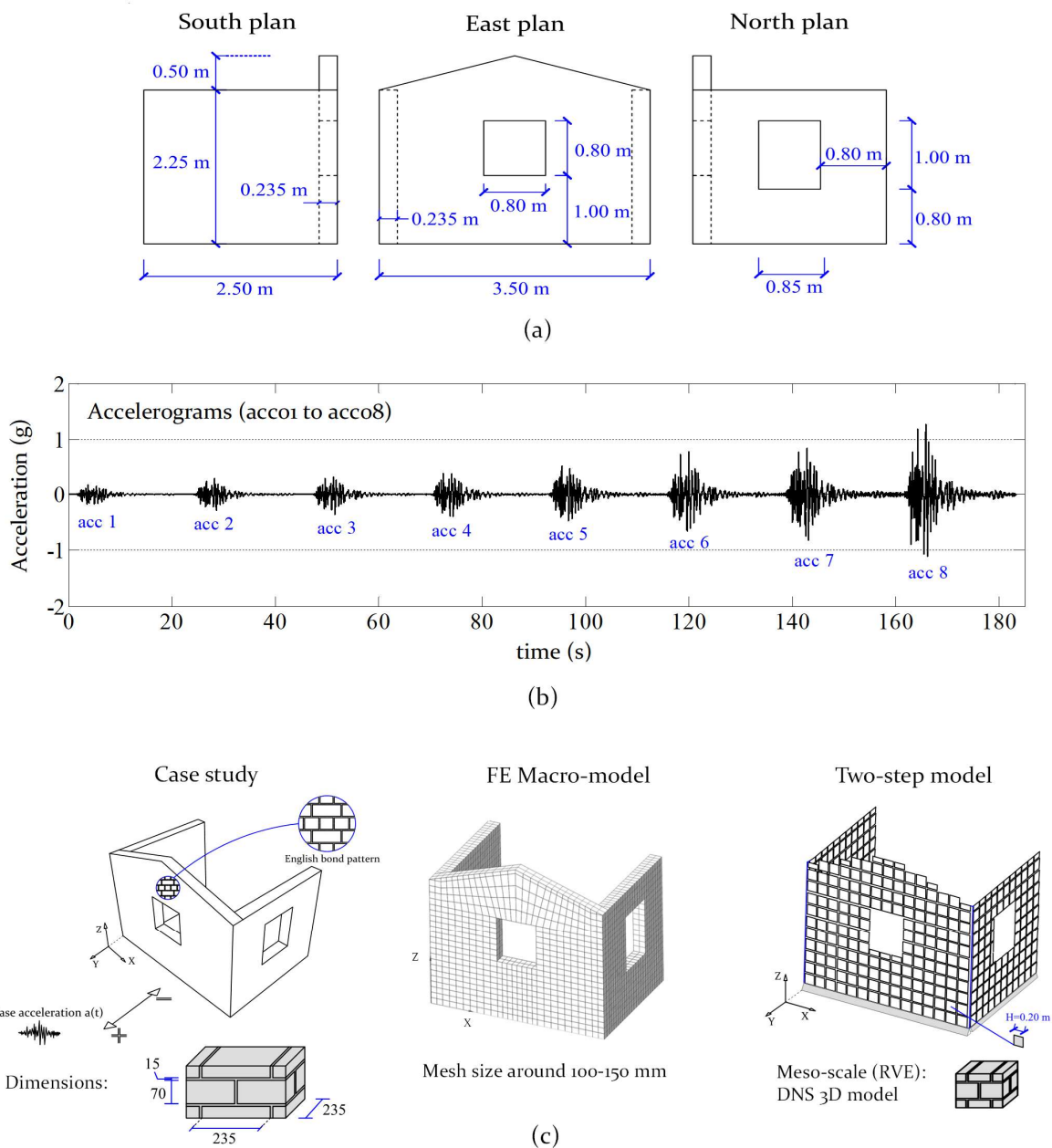
539 Where $t_m = 15 \text{ mm}$ is the thickness of the mortar joints; G_u and G_m are the shear modulus of the unit
 540 and mortar, respectively. Fig. 5b shows the obtained results. It is noticed that the presence of the vertical
 541 discontinuity in the masonry thickness has a marginal effect on the RVE vertical bending behavior M_{yy} .
 542 On the contrary, the model with the discontinuity manifests a lower capacity for both the horizontal M_{xx}
 543 and torsional M_{xy} moments with differences ranging the 33% and 17%, respectively. Additionally, if
 544 the KP model results are considered, an error of 52% is expected for the horizontal bending moment
 545 case. Such results prove the importance of addressing the mortar discontinuities and the three-
 546 dimensional shear effects along the thickness of a masonry wall; especially in cases where the thickness
 547 value is significant, as seen in (Silva et al. 2018). Also, this highlights the care that needs to be taken
 548 when adopting a modeling strategy for a given case study. The total processing time (CPU time
 549 requirements using a laptop with an i7-4710MQ CPU) of the simulations was 81 seconds, 246 seconds
 550 and 249 seconds for the KP model, DNS model without discontinuity and DNS model with
 551 discontinuity, respectively.

552 **4.2 Engineering complex problems: meso/macro scales**

553 **4.2.1 LNEC brick-house mock-up**

554 The selected case study outcomes from the experimental work performed in LNEC by Candeias et al.
 555 (2017), which was developed to foster a blind test prediction by different invited authors on the dynamic
 556 behavior of a masonry structure. The studied brick structure is composed of three walls in a U-shaped
 557 plan arrangement. The main façade (East plan) presents a gable wall and is linked with two transversal
 558 walls which act as abutments (North and South plans). These were constructed with clay brickwork in
 559 an English-bond arrangement of 235 mm of thickness (slenderness ratio about 1:10). The geometrical
 560 features are seen in Fig. 6a. The brick mock-up was tested up to collapse in a shaking table under a
 561 unidirectional seismic loading. The seismic input was applied in a perpendicular direction (E-W) to the
 562 main façade and derives from the N64E strong ground motion component associated with the February

563 21 of 2011 earthquake occurred in Christchurch, New Zealand. After the filtering and cropping, the
 564 latter time signal served as a reference for the seismic input generation and is composed of eight
 565 accelerograms. These have been obtained from a scaling process, starting from one up to three. The
 566 input signal considered in the dynamic analysis is displayed in Fig. 6b.



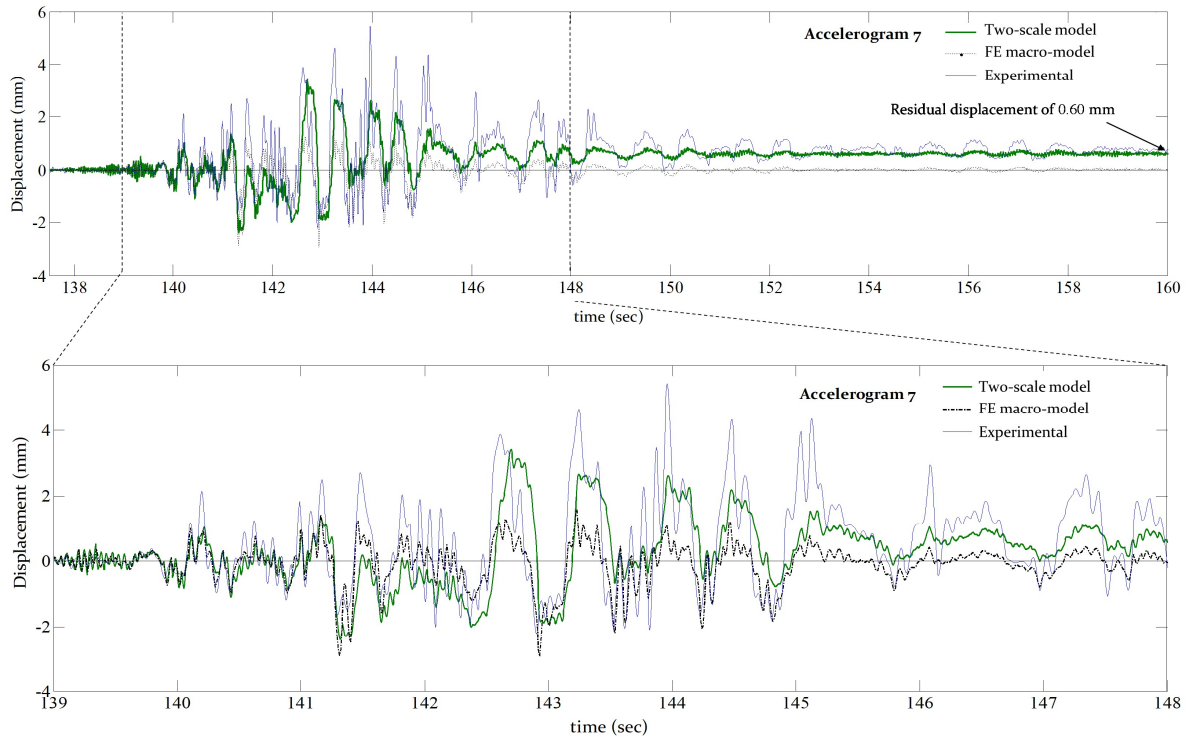
567 Fig. 6 – Case study: (a) the geometry of the case study; (b) the experimental input seismic signal; (c)
 568 case study and the numerical models considered for the dynamic analysis.
 569

570 Two (out of three) of the presented numerical approaches are used for this analysis as depicted in Fig.
 571 6c. In particular, the macroscopic model and the simplified two-scale model. Again, the former

572 represents masonry as an isotropic material and has been defined here to follow a total strain rotating
573 crack constitutive material model, whereas an exponential and parabolic law is adopted, respectively,
574 for the tensile and compressive behaviors. An approximated mesh size of 100 up to 150 mm was defined
575 using 3D finite elements, and such fine discretization intends to by-pass numerical problems faced
576 during the performed computations. For the latter, a direct numerical simulation (DNS 3D mode with
577 discontinuity) has been assumed at a meso-scale to derive the homogenized quantities, wherein the
578 vertical mortar discontinuity is present in the thickness direction. At a macro-scale, a mesh size of 200
579 mm is adopted.

580 The calibration of the elastic brickwork stiffnesses (E_{xx} , E_{xy} and E_{yy}) has been reached by accounting
581 with the modal identification data available. For the strength properties, as the tensile strength, cohesion,
582 and compressive strength, the values from (Candeias et al. 2017) have been used. The parameters that
583 control the material curves beyond the peak, namely the fracture energies, refer to typical masonry
584 literature values and no experimental reference is known.

585 Dynamic analysis has been performed by subjecting the structure to the defined seismic input. Since
586 the structure has collapsed for the last accelerogram (acc 8), the comparison is achieved for the
587 accelerogram seven (acc 7) as shown in Fig. 7. The results give good indications on the ability of the
588 presented two-step approach in the dynamic behavior prediction of the English-bond structure, as a
589 good agreement has been found with the experimental time-history displacements. Even if slight
590 differences are visible for the peak displacements, the two-scale model also accurately reproduces the
591 residual displacement.



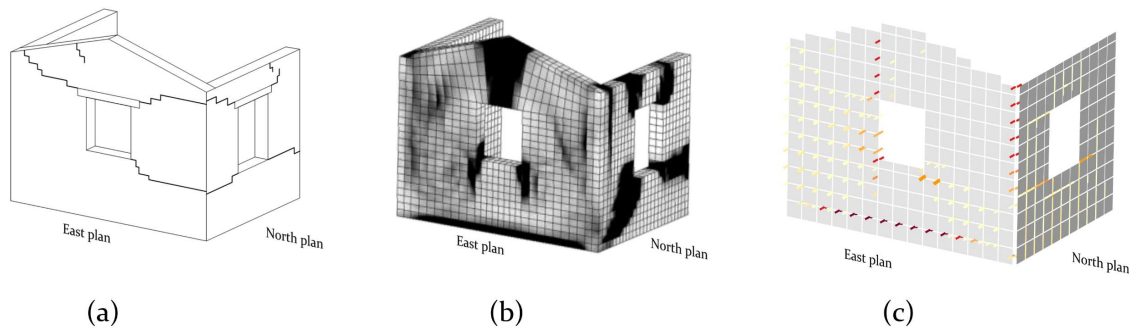
592

593 Fig. 7 – The obtained time-history displacements for the last analyzed accelerogram (acc 7).

594 On the other hand, the macroscopic model seems to overestimate the structure capacity. The response
 595 is far from being alike with the behavior reproduced by the latter procedure, despite sharing both the same
 596 material and mechanical input. The non-consideration of the existent vertical discontinuity seems to be
 597 of utmost importance. In fact, the latter is paramount as it decreases significantly the bending and
 598 torsional capacities. Furthermore, the macroscopic approach makes use of a hysteretic behavior with
 599 secant unloading-reloading branches, a feature that leads to the underestimation of the energy
 600 absorption and is incapable to record permanent plastic deformations.

601 Additionally, Fig. 8 reports the observed experimental and numerical damage maps. From the two-scale
 602 and macroscopic models, a vertical crack in the gable wall (due to horizontal bending) is observed. In
 603 the former, it is registered, as well, the onset of cracking due to torsional movements in the east plan
 604 opening towards the corners. Both strategies captured moderate damage in the east-north corner, even
 605 if this is not clear from the experimental observations. Some in-plane damage around the north piers is
 606 also registered. In general, a reasonable agreement has been found for such a complex study. The total

607 processing time (CPU time requirements using a laptop with an i7-4710MQ CPU) of the simulations
608 was 76 minutes and 720 min for the two-scale (DNS 3D) model and the FE macro-model, respectively.

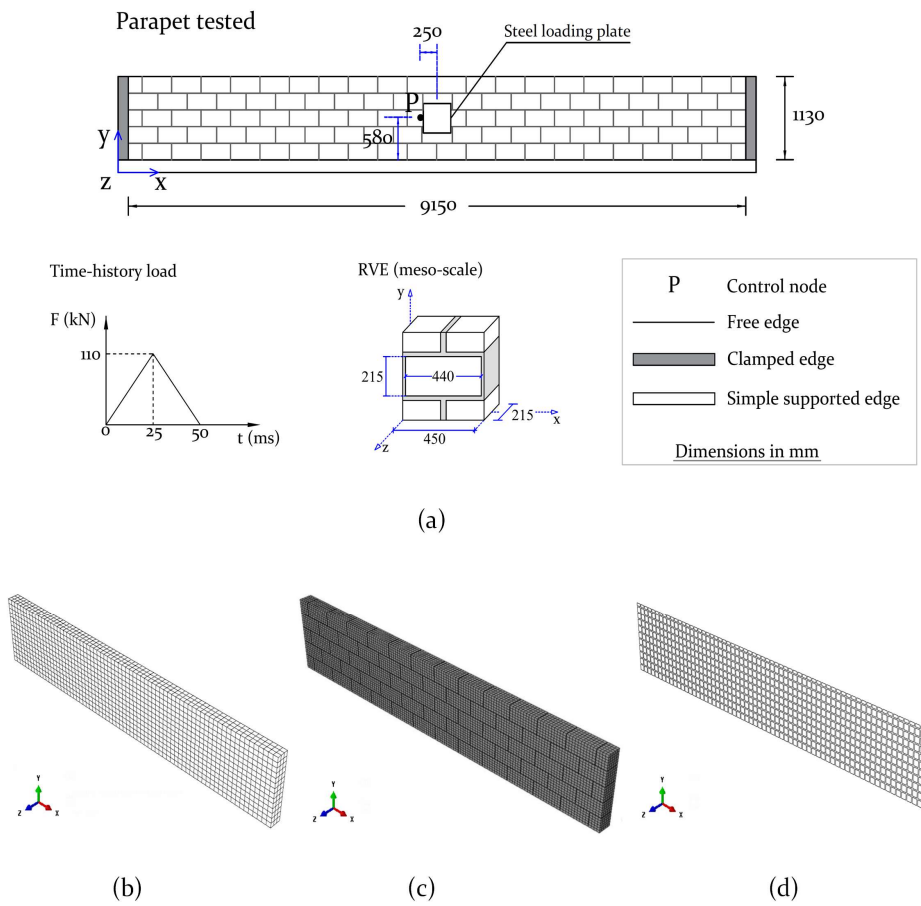


609
610 Fig. 8 – Observed damage: (a) after the experimental series of seven accelerograms (from acc 1 to acc
611 7); (b) for the macroscopic model at the instant $t = 160$ seconds; and (c) for the two-scale model at the
612 instant $t = 160$ seconds.

613 4.2.2 Sheffield university parapet wall

614 Experimental data available from the research reported by Gilbert et al. (2002a) is used to assess the
615 ability of the presented numerical strategies in the prediction of the dynamic behavior of masonry when
616 subjected to a low-velocity impact load. The numerical strategies presented in section 3 are addressed,
617 see Fig. 9a,b,c. Note that a finer mesh refinement has been assumed for all the strategies.

618 The selected parapets are designated as C6 and C7 and are replicates. Their assemblage was executed
619 with strong concrete blocks and weak mortar. The parapet walls and brick dimensions, as well as the
620 boundary conditions assumed, are reported in Fig. 9a. Aiming to model a vehicle-like impact at both
621 mid-height and length of the walls, a triangular time-history load distribution, in which the peak value
622 is equal to 110 kN, has been applied. The deformation of the studied parapets has been recorded in a
623 node located 580 mm above the base and deviated 250 mm from the center.



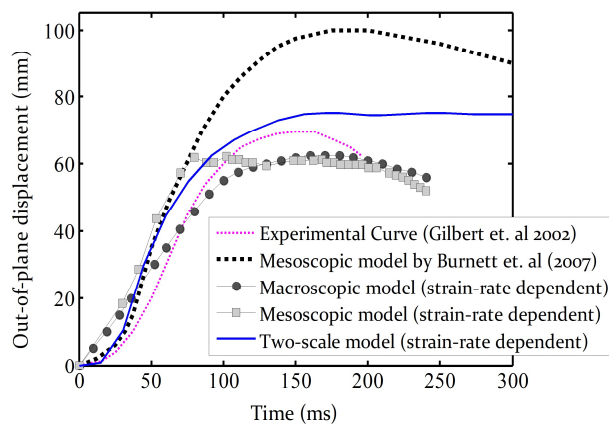
624

625 Fig. 9 – Sheffield university parapet Wall : (a) geometry of the running bond masonry parapets C6 and
 626 C7 tested by Gilbert et al. (2002a); and the numerical models presented by the authors that are used in
 627 this analysis, (b) the strain-rate FE macroscopic model (macro-model approach); (c) the strain-rate FE
 628 mesoscopic model (micro-modeling approach); and (d) the strain-rate two-scale homogenized-based
 629 model.

630 The static material properties and the rate-dependency issue is addressed for all the formulations; for
 631 the macroscopic model in (Rafsanjani et al. 2015a), for the mesoscopic model in (Rafsanjani et al.
 632 2015b), and for the two-scale model in (Silva et al. 2017a). To guarantee the consistency and
 633 representativeness of the comparison, the models used the same analytical expressions for the *DIFs*. In
 634 particular, the laws made available by Hao and Tarasov (2008), who studied the experimental dynamic
 635 behavior of a series of brick and mortar specimens under uniaxial compressive tests through a tri-axial
 636 static-dynamic apparatus. As information regarding the strain-rate effects on tensile and shear masonry
 637 properties is lacking, the *DIF* regression equations for the tensile and shear material parameters (as the

638 tensile ultimate strength σ_{t0_mortar} , mode-I fracture energy G_f^I , cohesion c and mode-II fracture energy
639 G_f^{II}) are assigned to be equal to the compressive ones.

640 The obtained results are analyzed in terms of displacement magnitude with respect to time. The
641 comparison is achieved through the experimental results (Gilbert et al. 2002) and complemented with
642 a mesoscopic strain-rate independent model by Burnett et al. (2007a). Fig. 10 shows that the curve from
643 (Burnett et al. 2007) leads to excessive displacements (and under stiff response). This author presented
644 a simplified FE mesoscopic model (micro-modeling approach) that represents mortar joints with
645 interface elements. This strategy is strain-rate independent, ergo their accuracy is highly dependent on
646 the static material properties adopted. The use of static strength properties instead of dynamic ones may
647 mislead the results, i.e. an underestimation of the collapse load may occur.



648

649 Fig. 10 – Time history of the out-of-plane displacement obtained for the control node of the parapets
650 C6 and C7 and deformed shapes observed with the proposed model for the time instants 0.5ms, 1.41ms,
651 25ms, and 300 ms.

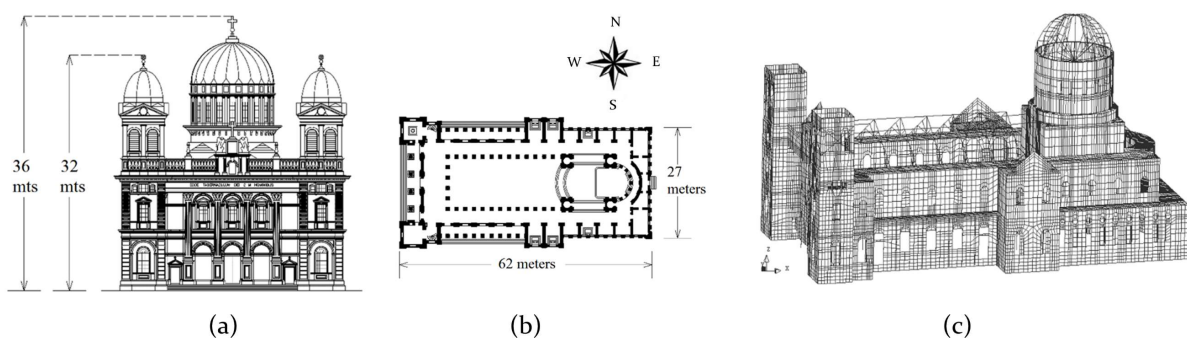
652 Conversely, the presented numerical models are reasonably accurate in predicting the peak
653 displacement, with a relative error of around 10%. Regarding the post-peak behavior, it is noticeable
654 that the structure displacement restitution of the two-scale model is practically inexistent. Yet, similarly
655 to the experimental results, the latter is not entirely reproduced by the other three numerical models
656 under comparison, presenting both an out-of-plane displacement that slightly decreases in post-peak
657 after the time instant of 180 mm. This is possibly due to the irreversible displacements computed
658 (permanent plastic strains) within the cyclic behavior of the CDP model. The response is still
659 remarkable. The total processing time (CPU time requirements using a laptop with an i7-4710MQ CPU)

660 of the simulations is 0.2 hours (12 minutes) for the two-scale (DNS 3D) model, 2.5 hours for the FE
661 macro-model, and 23 hours for the FE micro-model.

662 4.3 Engineering super large/complex problems: macro-scale

663 4.3.1 Cathedral of the Blessed Sacrament

664 The Cathedral of the Blessed Sacrament is located in Christchurch city (New Zealand). The building is
665 based on Roman-style and was built using Oamaru limestone. The geometrical features are briefly
666 addressed in Fig. 11a,b. The building suffered a strengthening intervention in 2004, in which the
667 structural safety level was assumed to be adequate. Yet, a sequence of four main seismic events over a
668 period of nine months, between 4 September 2010 and 13 June 2011, caused progressive damage and
669 local collapses of the two bell towers. Recognizing the symbolism and type of loss associated with this
670 Basilica, a numerical study has been conducted to evaluate potential retrofitting strategies that could
671 mitigate the extensive damage found and avoid the collapse of the bell towers. Two strengthening
672 proposals to be implemented in the Cathedral, considering the strengthening intervention of 2004, have
673 been analyzed. The goal is to guarantee the ultimate limit state (ULS), that is, to prevent the collapse of
674 structural elements for the highest mean horizontal PGA recorded in the 2010 and 2011 earthquakes.
675 Thus, the value assigned as performance reference for the structural assessment is given by 0.43 g and
676 is defined by the February 2011 seismic event (it corresponds to a period of return around 400 years for
677 new buildings design according to (NZS1170 2004)).



678 Fig. 11 – Geometry of Basilica of the Blessed Sacramento: (a) west elevation; (b) plan.
679

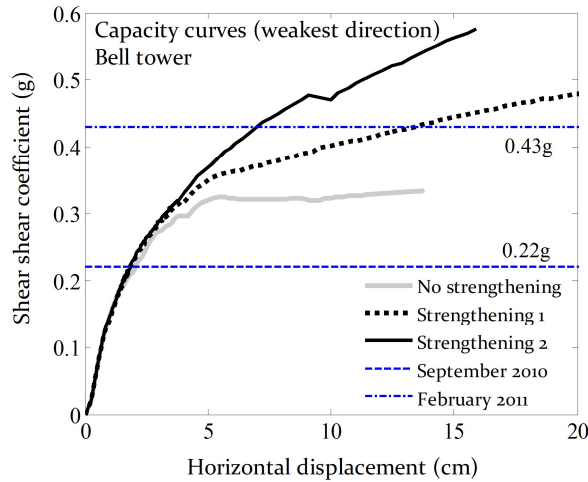
680 An FE numerical model was prepared using the presented continuum FE-based anisotropic model
681 (macro-modeling) implemented in the software DIANA (2017). A total-strain fixed crack model was
682 adopted to represent the physical nonlinear behavior. For such a large structure, aiming at reducing the

683 structural global number of degrees of freedom of the Basilica's numerical model, beam, shell and solid
684 finite elements were used. The final FE mesh of the Basilica's model is presented in Fig. 11c and
685 corresponds to a total number of 178,719 degrees of freedom. The material and mechanical properties
686 have been based on information provided by the NZ authorities and from literature, see (Silva et al.
687 2018) for more details.

688 The seismic performance of the Cathedral was evaluated through a pushover analysis. This is a time-
689 invariant analysis (static) and is more convenient than a nonlinear dynamic analysis with time
690 integration as it is computationally more attractive. A uniform pattern was adopted for the applied
691 horizontal loads meaning that the distribution of applied forces is proportional to the mass distribution
692 of the structure.

693 For the first strengthening proposal, a set of 12-meters long stainless-steel tie rods was applied to the
694 structure at the level of the floors being anchored in the slabs. The aim has been the improvement of
695 the connection between orthogonal walls, allowing a better force distribution into the nave walls and
696 preventing the out-of-plane collapse of the bell towers. The second strengthening proposal kept the
697 three tie rods of the first proposal at the main façade but includes ring beams at the bell towers instead
698 of the stainless-steel tie rods. Such addition aimed to improve the connection between structural
699 elements, namely the bell towers and nave walls. Furthermore, it intends to allow better confinement
700 for the bell towers in order to facilitate a better force distribution and prevent out-of-plane collapse.

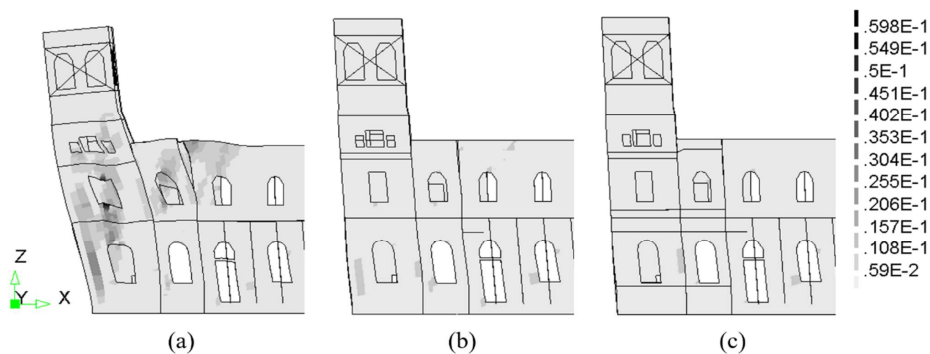
701 The efficiency of the strengthening proposals was evaluated based on the pushover analyses for the
702 longitudinal direction $-X$ only (the out-of-plane mechanism of the bell towers and main façade were
703 found in (Silva et al. 2018) to have the lowest load capacity). The capacity curves depicted in Fig. 12
704 shows a clear improvement in the load and inelastic displacement capacity of the structure, for which
705 at least a maximum horizontal load of about 0.57 g was obtained (strengthening proposal 2). The first
706 strengthening proposal allows at least a maximum horizontal load equal to 0.49 g. It is noted that the
707 maximum horizontal load applied to the non-strengthened model is equal to 0.35 g.



708

709 Fig. 12 – Obtained capacity curves with and without the strengthening proposals.

710 The damage assessment was evaluated based on the maximum principal tensile strain, which is a good
 711 qualitative indicator of cracking. The structural strengthening undertaken in 2004 played a decisive role
 712 in the avoidance of further damage, but this strengthening was insufficient to prevent local failure
 713 mechanisms. The crack pattern of the non-strengthened model shows that the Basilica suffered severe
 714 damage in both bell towers and in the vicinity walls for a horizontal load of 0.35 g (Fig. 13a). Extensive
 715 cracking due to in-plane shear failure is observed. Fig. 13b,c show that the results are in accordance
 716 with the intended one, as insignificant damage being observed at the bell tower walls. Hence, the
 717 strengthening measures distribute the loads to the nave walls and nave slabs, causing more damage to
 718 these elements, namely some cracks on the first floor of the nave.

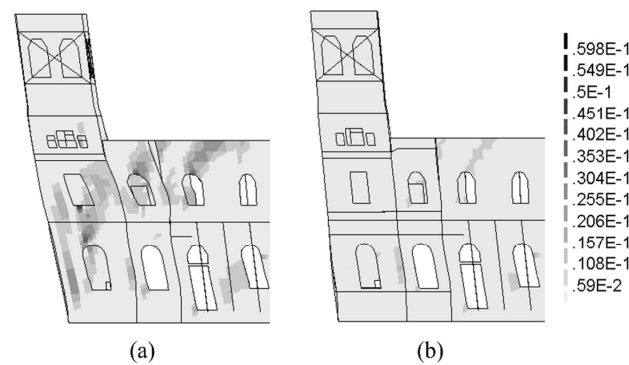


719

720 Fig. 13 – Comparison of principal tensile strains for the horizontal load equal to 0.35 g: (a) non-
 721 strengthened model; (b) strengthened model 1; (c) strengthened model 2.

722 Finally, the seismic performance of the structure accounting with the strengthening proposals was also
 723 evaluated for a horizontal load equal to 0.43 g (PGA of the February 2010 earthquake). Fig. 14 presents

724 the principal tensile strains, from which it can be observed that the model with the first strengthening
 725 scheme suffers more damage than the one with the second strengthening scheme. Thus, the first
 726 strengthening proposal is an effective solution as it creates new load paths and delays failure. However,
 727 it does not provide enough strengthening for the two-bell towers in order to change its condition as the
 728 most vulnerable elements of the structure. The second strengthening proposal, which includes stainless
 729 steel rings, presents the best seismic performance guaranteeing a safety level for the bell towers of at
 730 least 40% of the full code requirements (Silva et al. 2018).



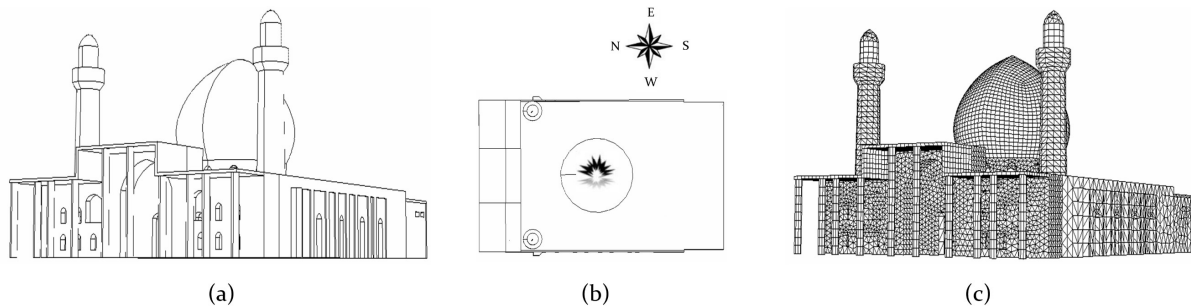
731
 732 Fig. 14 – Comparison of principal tensile strains for the horizontal load equal to 0.43 g: (a) strengthened
 733 model 1; (b) strengthened model 2.

734 The structural strengthening undertaken in 2004 played a decisive role in the avoidance of further
 735 damage, but it was insufficient to prevent local failure mechanisms. The numerical results indicate that
 736 the structure is unsafe for an earthquake such as the one experienced in February 2011, in which the
 737 collapse of the bell towers and significant damage would be expected. The model allowed the
 738 identification of two possible strengthening solutions that could change the outcome of similar seismic
 739 events to be addressed. The total processing time (CPU time requirements using a laptop with an i7-
 740 4710MQ CPU) of the simulations is around 14 hours for the non-strengthened numerical model
 741 accounting with the full structure.

742 4.3.2 Al-Askari Holy Shrine: blast load

743 The Islamic cultural heritage site of Al-Askari holy shrine is situated in Samarra (Iraq) and its geometry
 744 is shown in Fig. 15a. The Al-Askari shrine suffered a terrorist attack in February 2006. A large quantity
 745 of explosive charge (200 kg TNT) has been placed at the top of the dome by taking advantage of the
 746 existing scaffold due to the ongoing conservation works (Pandey et al. 2006). The blast load destroyed

747 the dome and the resulting debris damaged the buildings' roof. The majority of the dome's structure
748 collapsed inside the mosque according to (Baylot and Bevins 2007). Also, significant damage has been
749 reported in both the East and West façades (Fig. 15b).



750
751 Fig. 15 – Islamic cultural heritage site of Al-Askari holy shrine: (a) geometry; (b) local where the blast
752 detonation took place, i.e. placed at the top of the dome; and (c) FE mesh adopted for the continuum
753 macroscopic model.

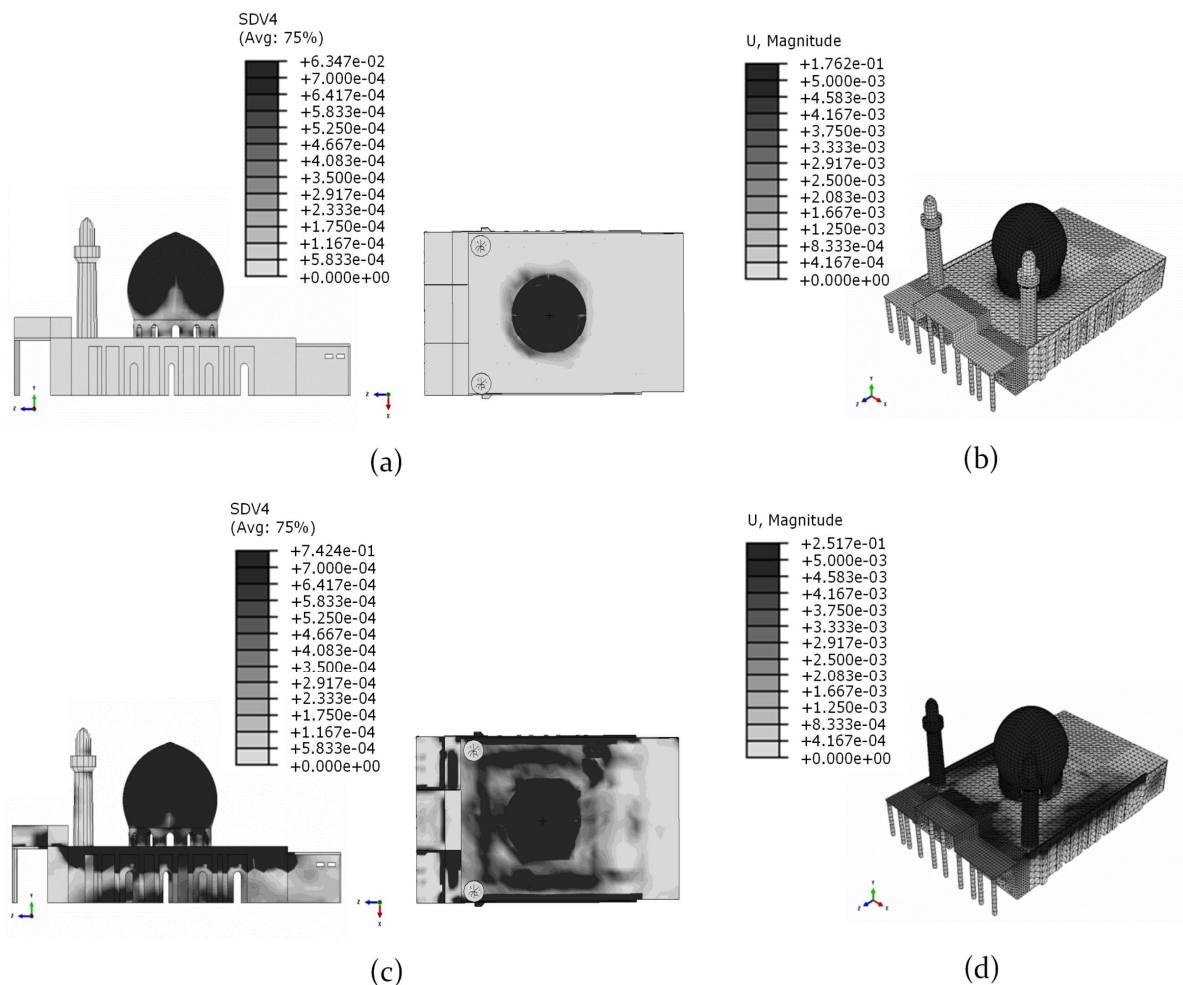
754 The continuous anisotropic FE macro-model with strain-rate dependency, presented in section 3.2, has
755 been used in this study. The main goal is the demonstration of the capability that the proposed advanced
756 numerical tool (meaning the plasticity model) offers in the analysis of full masonry structures under
757 blast load. In this regard, a numerical model featuring the structure of the mosque has been developed
758 in ABAQUS (2013). The supports have been defined as fixed and only solid FEs have been used; i.e.
759 8-noded linear bricks (reduced integration, hourglass control) and 4-node linear tetrahedron. The final
760 model has a total of 112,623 degrees of freedom and the FE mesh is represented in Fig. 15c.

761 The material anisotropy has been considered following adequate literature information, see (Rafsanjani
762 2015). To account with the strain-rate dependency of the masonry composite yield surface, the required
763 DIF laws from the study by (Pereira and Lourenço 2016a) have been used. In order to keep the problem
764 with a pure Lagrange formulation, the blast load has been applied as pressure load profiles applied in
765 different zones of the building to assure the representativeness of its distribution. A total of eight zones
766 with different stand-off distances have been modeled. The results of the dynamic analysis are shown
767 next in terms of contour plots for two instant times t .

768 For a time instant equal to $t = 25 \text{ ms}$, i.e. immediately after the occurrence of the explosion (that occurs
769 for a $t = 20 \text{ ms}$), the maximum principal plastic strain is given in Fig. 16a. Significant values are
770 localized in the dome, whereas the incremental deformed shape of Fig. 16b shows displacements in the

771 order of 17 cm. The level of loading seems high enough for this structure hence severe non-linearity for
 772 the masonry behavior and consequently, intense crack formation is reported. Note that the plasticity
 773 model does not have incorporated a damage model, yet the plastic strains could be a good qualitative
 774 indicator of damage.

775 The onset of significant damage is visible in the top of the dome but instantly includes its bottom part
 776 around the openings. Due to the inertial forces, the dome continues to move during the unloading phase
 777 and other parts of the structure, as the roof, minarets, and side facades, are affected. This is addressed
 778 in Fig. 16c, where the maximum principal strain obtained is plotted for $t = 70\text{ ms}$, i.e. after the
 779 occurrence of the blast and the most significant over-pressures profiles. It is clear now that the damage
 780 is more spread in the latter elements, as supported by the incremental deformed shape of Fig. 16d.



781

782 Fig. 16 – Results obtained for the Islamic cultural heritage site of Al-Askari after the numerical analysis
 783 of a blast load: (a) maximum principal plastic strain after the blast load ($t=25\text{ms}$); (b) incremental
 784 deformed shape (SI unit, m) after the blast load ($t=25\text{ms}$); (c) maximum principal plastic strain after the

785 most significant over-pressure profiles ($t=70\text{ms}$); incremental deformed shape (SI unit, m) after the
786 most significant over-pressure profiles ($t=70\text{ms}$).

787 The qualitative evaluation of the damage is presented in detail in (Rafsanjani 2015). It has been
788 concluded that the damage pattern found certainly leads to the collapse of the dome and to extensive
789 degradation of both the East and West façades. The addressed conclusions go hand in hand with the
790 reported real behavior, ergo proving the adequacy of the advanced strain-rate FE macroscopic model.
791 One may note, however, that the application of the blast load can be a cumbersome task, as
792 demonstrated by other studies (Baylot and Bevins 2007). The total processing time (CPU time
793 requirements using a laptop with an i7-4710MQ CPU) of the simulation is 101 hours.

794 **5 Final remarks**

795 FE-based numerical strategies have nowadays a primary role in the mechanical behavior analysis of
796 masonry structures. Its usefulness is barely questioned, as these are used daily by both the academic
797 and professional communities to solve problems within manageable timelines that otherwise would
798 defy treatment (Linz 1988). Since computational modeling relies on the physical insight of materials,
799 further developments are continuously needed aiming to decrease the related epistemic and modeling
800 uncertainties.

801 In such a context, the present paper addressed the importance of computational strategies for the
802 numerical analysis of masonry structures. Three advanced FE-based models have been proposed and
803 include an FE micro-model, an FE macro-model, and a novel simplified FE² multi-scale model. These
804 models can reproduce the masonry orthotropy, full softening behavior, and loading strain-rate
805 dependency.

806 The proposed strategies have been used for the engineering of small to large, super-large and complex
807 problems with a focus on the well-known out-of-plane vulnerability of unreinforced masonry structures.

808 The evaluated case studies are the following ones: (i) meso-scale static characterization of the out-of-
809 plane behavior for an English-bond masonry wall; (ii) seismic analysis of the LNEC brick house
810 prototype and the Cathedral of the Blessed Sacrament; (iii) impact load analysis of the Sheffield
811 university parapet wall; and (iv) the blast load analysis of the Al-askary Holy Shrine.

812 The small-scale problem included the characterization of the out-of-plane homogenized behavior of an
813 English-bond masonry bond at a meso-scale. The results proved that the mid-thickness vertical joint of
814 an English-bond masonry wall leads to the reduction of its out-of-plane capacity. A reduction of 33%
815 and 17% was found for the horizontal bending and torsional moment peak values, respectively, between
816 a three-dimensional numerical model with and without the discontinuity. This effect has been also
817 witnessed for the large-scale study of the LNEC brick house mockup. Here, a good agreement between
818 the experimental dynamic response and the one predicted by the simplified multi-scale strategy was
819 found. The FE macro-modeling strategy is, however, unable to capture the lessening of the masonry
820 bending strength and hence to properly predict the structure's behavior when subjected to a seismic
821 load; expected as it assumes an isotropic behavior for the homogeneous equivalent material.

822 Concerning the complex problem of the Sheffield university parapet wall subjected to an impact load,
823 a good resemble was achieved for all the proposed strategies. A maximum relative error of 10% was
824 found for the out-of-plane displacement of the control node. This error is, however, only achievable
825 since the three proposed models account with the strain-rate dependency of the masonry by dynamic
826 increase factors (DIFs). It has been shown that static material and mechanical properties do not offer
827 adequate insight into the masonry response for fast dynamic problems.

828 For the super-large and complex problems, as the Cathedral of Blessed Sacrament and the Al-askari
829 Holy Shrine case studies, the use of an FE macro-model seemed to be the most convenient one as it
830 allows a most straightforward modeling stage. Regarding the former, the numerical model allowed to
831 predict the proneness to collapse of the two bell towers of the Cathedral when subjected to the
832 Christchurch seismic events of 2010 and 2011; but, as well, to compare the efficiency of two-retrofitted
833 interventions. Regarding the latter, the FE macro-model allowed to predict well the collapse of the main
834 dome and capture the severe damage found in both the East and West façades of the Mosque when
835 subjected to a blast load. Although an FE macro-modeling approach is very practical, some attention is
836 recommended when a more detailed description of the response, damage onset, and propagation is
837 desired for a given structural element, as concluded by the obtained smeared damage in the latter
838 problems. In such cases, down-scaling through a micro-modeling or a multi-scale approach could be a
839 proper alternative.

840 From the conducted analyses it is noteworthy to address that the modeling strategies adopted for the
841 mechanical study of periodic masonry are mainly dependent on the dimensions of the structure under
842 investigation. For meso-scale problems (order of centimeter), a purely micro-modeling approach seems
843 preferable. Yet, for large or super-large problems (order of meters), as the study of the dynamic behavior
844 of a structural wall or building, the use of a macro-modeling or simplified multi-scale approach is
845 generally followed. In such cases, the potential of a simplified multi-scale model and the inadequacy of
846 an FE micro-model is especially clear for the Sheffield university parapet wall case study. From a
847 computational standpoint, the former is 115 times faster than the FE-micro model and 12.5 times faster
848 than a continuous FE macro-model.

849 Through a logical extension, a simplified multi-scale approach can significantly decrease the CPU times
850 obtained when using an FE macro-model in the study of super large and complex problems. For
851 instance, the CPU time of 14 hours and 101 hours obtained using an FE macro model for the Al-the
852 Cathedral of the Blessed Sacrament and the Al-Askari Holy Shrine Mosque case studies, respectively.
853 Even though, it is important to address that the modeling step of such structures using the proposed
854 multi-scale model, through a discrete-based strategy, can be also cumbersome. Hence, the decision of
855 the best strategy should account with the trade-off between the required time for the numerical model
856 preparation and the numerical analysis.

857 Lastly, the authors stress that the presented FE computational strategies have been implemented in
858 powerful advanced FE software's, as DIANA (2017) and ABAQUS (2013). The latter software is
859 already able to handle parallel computing and thus decrease the required running processing times of
860 the analysis (more evident in large-scale/complex problems). This is an important feature, as it has been
861 seen that the engineering solutions are largely conditioned by the required computational cost associated
862 with the modeling approach followed. Perhaps in a near future, when more powerful computers are of
863 common use (as quantum computers), the engineering of a given problem through a full continuous
864 micro-modeling approach from the meso- to a structural-scale will be, even if contentious from the
865 number of input parameters that demand, feasible from a CPU time standpoint.

866 **Acknowledgments**

867 This work was partly financed by FEDER funds through the Competitivity Factors Operational
868 Programme - COMPETE and by national funds through FCT – Foundation for Science and Technology
869 within the scope of the project POCI-01-0145-FEDER-007633.

870 **References**

871 ABAQUS. Finite Element Analysis (Theory Manual). Release 6.6 (software). Providence: RI: *Dassault*
872 *Systèmes Simulia Corporation*, 2013.

873 Adam, Jose M, Antonio Brencich, Tim G Hughes, and Tony Jefferson. Micromodelling of Eccentrically
874 Loaded Brickwork: Study of Masonry Wallettes. *Engineering Structures* **32** (5): 1244–51, 2010,
875 DOI: <https://doi.org/https://doi.org/10.1016/j.engstruct.2009.12.050>.

876 Anthoine, A. Derivation of the In-Plane Elastic Characteristics of Masonry through Homogenization
877 Theory. *International Journal of Solids and Structures* **32** (2): 137–63, 1995, DOI:
878 [https://doi.org/10.1016/0020-7683\(94\)00140-R](https://doi.org/10.1016/0020-7683(94)00140-R).

879 Baylot, James T., Billy Bullock, Thomas R. Slawson, and Stanley C. Woodson. Blast Response of
880 Lightly Attached Concrete Masonry Unit Walls. *Journal of Structural Engineering* **131** (8): 1186–
881 93, 2005, DOI: [https://doi.org/10.1061/\(ASCE\)0733-9445\(2005\)131:8\(1186\)](https://doi.org/10.1061/(ASCE)0733-9445(2005)131:8(1186)).

882 Baylot, James T, and Tommy L Bevins. Effect of Responding and Failing Structural Components on
883 the Airblast Pressures and Loads on and inside of the Structure. *Computers & Structures* **85** (11):
884 891–910, 2007, DOI: <https://doi.org/https://doi.org/10.1016/j.compstruc.2007.01.001>.

885 Bažant, Zdeněk P., and B. H. Oh.. Crack Band Theory for Fracture of Concrete. *Matériaux et*
886 *Constructions* **16** (3): 155–77, 1983, DOI: <https://doi.org/10.1007/BF02486267>.

887 Bažant, Zdeněk P., Yuyin Xiang, and Pere C. Prat.. Microplane Model for Concrete. I: Stress-Strain
888 Boundaries and Finite Strain. *Journal of Engineering Mechanics* **122** (3): 245–54, 1996, DOI:
889 [https://doi.org/10.1061/\(ASCE\)0733-9399\(1996\)122:3\(245\)](https://doi.org/10.1061/(ASCE)0733-9399(1996)122:3(245)).

890 Berto, Luisa, Anna Saetta, Roberto Scotta, and Renato Vitaliani. An Orthotropic Damage Model for
891 Masonry Structures. *International Journal for Numerical Methods in Engineering* **55** (2): 127–57,
892 2002, DOI: <https://doi.org/10.1002/nme.495>.

893 Blanco, Pablo J., Pablo J. Sánchez, Eduardo A. de Souza Neto, and Raúl A. Feijóo. Variational
894 Foundations and Generalized Unified Theory of RVE-Based Multiscale Models. *Archives of*

895 *Computational Methods in Engineering* **23** (2): 191–253, 2016, DOI:
896 <https://doi.org/10.1007/s11831-014-9137-5>.

897 Borst, René de, Joris J C Remmers, and Alan Needleman. Mesh-Independent Discrete Numerical
898 Representations of Cohesive-Zone Models. *Engineering Fracture Mechanics* **73** (2): 160–77,
899 2006, DOI: <https://doi.org/https://doi.org/10.1016/j.engfracmech.2005.05.007>.

900 Buchan, P A, and J F Chen. Blast Resistance of FRP Composites and Polymer Strengthened Concrete
901 and Masonry Structures – A State-of-the-Art Review. *Composites Part B: Engineering* **38** (5):
902 509–22, 2006, DOI: <https://doi.org/https://doi.org/10.1016/j.compositesb.2006.07.009>.

903 Buhan, Patrick de, and Gianmarco de Felice. A Homogenisation Approach to the Ultimate Strength of
904 Brick Masonry. *Journal of the Mechanics and Physics of Solids* **45** (7): 1085–1104, 1996, DOI:
905 [https://doi.org/10.1016/S0022-5096\(97\)00002-1](https://doi.org/10.1016/S0022-5096(97)00002-1).

906 Burnett, S., M. Gilbert, T. Molyneaux, G. Beattie, and B. Hobbs. The Performance of Unreinforced
907 Masonry Walls Subjected to Low-Velocity Impacts: Finite Element Analysis. *International*
908 *Journal of Impact Engineering* **34** (8): 1433–50, 2007, DOI:
909 <https://doi.org/10.1016/j.ijimpeng.2006.08.004>.

910 Calì, Ivo, Massimo Marletta, and Bartolomeo Pantò. A New Discrete Element Model for the
911 Evaluation of the Seismic Behaviour of Unreinforced Masonry Buildings. *Engineering Structures*
912 **40** (July): 327–38, 2012, DOI: <https://doi.org/10.1016/j.engstruct.2012.02.039>.

913 Calvi, G.M., Rui Pinho, G. Magenes, J.J. Bommer, L.F. Restrepo-Vélez, and H. Crowley. Development
914 of Seismic Vulnerability Assessment Methodologies over the Past 30 Years. *ISET Journal of*
915 *Eathquake Technology* **43** (3): 75–104, 2006.

916 Candeias, P. X., A. Campos Costa, N. Mendes, A. A. Costa, and P. B. Lourenço. Experimental
917 Assessment of the Out-of-Plane Performance of Masonry Buildings Through Shaking Table
918 Tests.” *International Journal of Architectural Heritage* **11** (1): 1–28, 2017, DOI:
919 <https://doi.org/10.1080/15583058.2016.1238975>.

920 Casolo, Siro. Rigid Element Model for Non-Linear Analysis of Masonry Façades Subjected to out-of-
921 Plane Loading. *Communications in Numerical Methods in Engineering* **15** (7): 457–68, 1999.

922 Casolo, Siro, and Gabriele Milani. A Simplified Homogenization-Discrete Element Model for the Non-

923 Linear Static Analysis of Masonry Walls out-of-Plane Loaded. *Engineering Structures* **32** (8):
924 2352–66, 2010, DOI: <https://doi.org/10.1016/j.engstruct.2010.04.010>.

925 Casolo, Siro, and Giuseppina Uva. Nonlinear Analysis of Out-of-Plane Masonry Façades: Full Dynamic
926 versus Pushover Methods by Rigid Body and Spring Model. *Earthquake Engineering & Structural*
927 *Dynamics* **42** (4): 499–521, 2013, DOI: <https://doi.org/10.1002/eqe.2224>.

928 Cecchi, A., and G. Milani. A Kinematic FE Limit Analysis Model for Thick English Bond Masonry
929 Walls. *International Journal of Solids and Structures* **45** (5): 1302–31, 2008, DOI:
930 <https://doi.org/10.1016/j.ijsolstr.2007.09.019>.

931 Cecchi, Antonella, and Karam Sab. Out of Plane Model for Heterogeneous Periodic Materials: The
932 Case of Masonry. *European Journal of Mechanics - A/Solids* **21** (5): 715–46, 2002, DOI:
933 [https://doi.org/10.1016/S0997-7538\(02\)01243-3](https://doi.org/10.1016/S0997-7538(02)01243-3).

934 Cervera, M, and M Chiumenti. Mesh Objective Tensile Cracking via a Local Continuum Damage
935 Model and a Crack Tracking Technique. *Computer Methods in Applied Mechanics and*
936 *Engineering* **196** (1–3): 304–20, 2006, DOI: <https://doi.org/10.1016/j.cma.2006.04.008>.

937 Cundall, PA, and P. Hart. A Computer Model for Simulating Progressive Large Scale Movements in
938 Blocky Rock Systems. *In Proc. Symp. Rock Fracture (ISRM)*, vol. **1**:II–8. Nancy, France, 1971.

939 D’Ayala, D., and E. Speranza. Definition of Collapse Mechanisms and Seismic Vulnerability of
940 Historic Masonry Buildings. *Earthquake Spectra* **19** (3): 479–509, 2003, DOI:
941 <https://doi.org/10.1193/1.1599896>.

942 D’Ayala, Dina, and Yanan Shi. Modeling Masonry Historic Buildings by Multi-Body Dynamics.
943 *International Journal of Architectural Heritage* **5** (4–5): 483–512, 2011, DOI:
944 <https://doi.org/10.1080/15583058.2011.557138>.

945 Dennis, Scott T., James T. Baylot, and Stanley C. Woodson. Response of 1/4-Scale Concrete Masonry
946 Unit (CMU) Walls to Blast. *Journal of Engineering Mechanics* **128** (2): 134–42, 2002, DOI:
947 [https://doi.org/10.1061/\(ASCE\)0733-9399\(2002\)128:2\(134\)](https://doi.org/10.1061/(ASCE)0733-9399(2002)128:2(134)).

948 Dhanasekar, M, PW Kleeman, and AW Page. The Failure of Brick Masonry under Biaxial Stresses.
949 *Proceedings of the Institution of Civil Engineers* **79** (2): 295–313, 1985, DOI:
950 <https://doi.org/10.1680/iicep.1985.992>.

951 DIANA, TNO. User's Manual Version 10.2, Delft, The Netherlands. BV, Delft, The Netherlands: *TNO*
952 *DIANA* 10.2, 2017.

953 Duvaut, G., and J.L. Lions. *Les Inéquations En Mécanique et En Physique*. Edited by Paris Dunod. New
954 York, 1972.

955 Frankie, Thomas M., Bora Gencturk, and Amr S. Elnashai. Simulation-Based Fragility Relationships
956 for Unreinforced Masonry Buildings. *Journal of Structural Engineering* **139** (3): 400–410, 2013,
957 DOI: [https://doi.org/10.1061/\(ASCE\)ST.1943-541X.0000648](https://doi.org/10.1061/(ASCE)ST.1943-541X.0000648).

958 Geers, M.G.D., V.G. Kouznetsova, and W.A.M. Brekelmans. Multi-Scale Computational
959 Homogenization: Trends and Challenges. *Journal of Computational and Applied Mathematics*
960 **234** (7): 2175–82, 2010, DOI: <https://doi.org/10.1016/j.cam.2009.08.077>.

961 Geogin, J.F., and J.M. Reynouard. Modeling of Structures Subjected to Impact: Concrete Behaviour
962 under High Strain Rate. *Cement and Concrete Composites* **25** (1): 131–43, 2003, DOI:
963 [https://doi.org/10.1016/S0958-9465\(01\)00060-9](https://doi.org/10.1016/S0958-9465(01)00060-9).

964 Giambanco, Giuseppe, Santi Rizzo, and Roberto Spallino. Numerical Analysis of Masonry Structures
965 via Interface Models. *Computer Methods in Applied Mechanics and Engineering* **190** (49–50):
966 6493–6511, 2001, DOI: [https://doi.org/10.1016/S0045-7825\(01\)00225-0](https://doi.org/10.1016/S0045-7825(01)00225-0).

967 Gilbert, M, B Hobbs, and T.C.K Molyneaux. The Performance of Unreinforced Masonry Walls
968 Subjected to Low-Velocity Impacts: Experiments. *International Journal of Impact Engineering*
969 **27** (3): 231–51, 2002, DOI: [https://doi.org/10.1016/S0734-743X\(01\)00049-5](https://doi.org/10.1016/S0734-743X(01)00049-5).

970 Grassl, Peter, and Milan Jirásek. Damage-Plastic Model for Concrete Failure. *International Journal of*
971 *Solids and Structures* **43** (22): 7166–96, 2006, DOI: <https://doi.org/10.1016/j.ijsolstr.2006.06.032>.

972 Greco, Fabrizio, Lorenzo Leonetti, Raimondo Luciano, and Patrizia Trovalusci. Multiscale Failure
973 Analysis of Periodic Masonry Structures with Traditional and Fiber-Reinforced Mortar Joints.
974 *Composites Part B: Engineering* **118**: 75–95, 2017, DOI:
975 <https://doi.org/https://doi.org/10.1016/j.compositesb.2017.03.004>.

976 Griffith, MC, and G Magenes. Evaluation of Out-of-Plane Stability of Unreinforced Masonry Walls
977 Subjected to Seismic Excitation. *Journal of Earthquake Engineering* **7** (141): 141–69, 2003.

978 Guragain, Ramesh, Kawin Worakanchana, Paola Mayorca, and Kimiro Meguro. Simulation of Brick

979 Masonry Wall Behavior Under Cyclic Loading Using Applied Element Method. *JSCE Structural*
980 *Engineering/Earthquake Engineering* **58** (6): 531–34, 2006, DOI:
981 <https://doi.org/10.11188/seisankenkyu.58.531>.

982 Hao, H, and BG Tarasov. Experimental Study of Dynamic Material Properties of Clay Brick and Mortar
983 at Different Strain Rates. *Australian Journal of Structural Engineering* **8** (2): 117, 2008.

984 Hao, Y., and H. Hao. Numerical Investigation of the Dynamic Compressive Behaviour of Rock
985 Materials at High Strain Rate. *Rock Mechanics and Rock Engineering* **46** (2): 373–88, 2013, DOI:
986 <https://doi.org/10.1007/s00603-012-0268-4>.

987 Hao, Y., H. Hao, and Z.X. Li. Influence of End Friction Confinement on Impact Tests of Concrete
988 Material at High Strain Rate. *International Journal of Impact Engineering* **60**: 82–106, 2013, DOI:
989 <https://doi.org/10.1016/j.ijimpeng.2013.04.008>.

990 Hendry, Emeritus A W. Masonry Walls: Materials and Construction. *Construction and Building*
991 *Materials* **15** (8): 323–30, 2001, DOI: [https://doi.org/https://doi.org/10.1016/S0950-](https://doi.org/https://doi.org/10.1016/S0950-0618(01)00019-8)
992 0618(01)00019-8.

993 Herbert, D. M., D. R. Gardner, M. Harbottle, and T. G. Hughes. Uniform Lateral Load Capacity of
994 Small-Scale Masonry Wall Panels. *Materials and Structures* **47** (5): 805–18, 2014, DOI:
995 <https://doi.org/10.1617/s11527-013-0092-7>.

996 Hill, R. A Self-Consistent Mechanics of Composite Materials. *Journal of the Mechanics and Physics*
997 *of Solids* **13** (4): 213–22, 1965, DOI: [https://doi.org/10.1016/0022-5096\(65\)90010-4](https://doi.org/10.1016/0022-5096(65)90010-4).

998 Kawai, Tadahiko. New Discrete Models and Their Application to Seismic Response Analysis of
999 Structures. *International Journal of Nuclear Engineering and Design* **48** (1): 207–29, 1978, DOI:
1000 [https://doi.org/10.1016/0029-5493\(78\)90217-0](https://doi.org/10.1016/0029-5493(78)90217-0).

1001 Konstantinidis, D, and N Makris. The Dynamics of a Rocking Block in Three Dimensions. *Proceedings*
1002 *of the 8th HSTAM International Congress on Mechanics*, 12–14, 2007.

1003 Lagomarsino, Sergio, Andrea Penna, Alessandro Galasco, and Serena Cattari. TREMURI Program: An
1004 Equivalent Frame Model for the Nonlinear Seismic Analysis of Masonry Buildings. *Engineering*
1005 *Structures* **56** (November): 1787–99, 2013, DOI: <https://doi.org/10.1016/j.engstruct.2013.08.002>.

1006 Lee, Jeeho, and Gregory L. Fenves. Plastic-Damage Model for Cyclic Loading of Concrete Structures.

1007 *Journal of Engineering Mechanics* **124** (8): 892–900, 1998, DOI:
1008 [https://doi.org/10.1061/\(ASCE\)0733-9399\(1998\)124:8\(892\)](https://doi.org/10.1061/(ASCE)0733-9399(1998)124:8(892)).

1009 Lemos, José V. Discrete Element Modeling of Masonry Structures. *International Journal of*
1010 *Architectural Heritage* **1** (2): 190–213, 2007, DOI: <https://doi.org/10.1080/15583050601176868>.

1011 Leonetti, L., Patricia Trovalusci, and Antonella Cechi. A Multiscale/Multidomain Model for the Failure
1012 Analysis of Masonry Walls: A Validation with a Combined FEM/DEM Approach. *International*
1013 *Journal for Multiscale Computational Engineering* **16** (4): 325–43, 2018, DOI:
1014 <https://doi.org/10.1615/IntJMultCompEng.2018026988>.

1015 Linz, Peter. A Critique of Numerical Analysis. *Bulletin of the American Mathematical Society* **19**:
1016 407–416, 1998, DOI: <https://doi.org/https://doi.org/10.1090/S0273-0979-1988-15682-0>.

1017 Lotfi, Hamid R., and P. Benson Shing. Interface Model Applied to Fracture of Masonry Structures.
1018 *Journal of Structural Engineering* **120** (1): 63–80, 1994, DOI:
1019 [https://doi.org/10.1061/\(ASCE\)0733-9445\(1994\)120:1\(63\)](https://doi.org/10.1061/(ASCE)0733-9445(1994)120:1(63)).

1020 Lourenço, P.B. Computational Strategies for Masonry Structures, PhD, Delft University of Technology,
1021 Delft, The Netherlands, 1196.

1022 Lourenço, P.B. An Anisotropic Macro-Model for Masonry Plates and Shells: Implementation and
1023 Validation. *TNO Building and Construction Research - Computational Mechanics*, report no.
1024 03.21.1.31.07: 34–91, 1997.

1025 Lourenço, P.B. Anisotropic Softening Model for Masonry Plates and Shells. *Journal of Structural*
1026 *Engineering* **126** (9): 1008–16, 2000, DOI: [https://doi.org/10.1061/\(ASCE\)0733-](https://doi.org/10.1061/(ASCE)0733-9445(2000)126:9(1008))
1027 [9445\(2000\)126:9\(1008\)](https://doi.org/10.1061/(ASCE)0733-9445(2000)126:9(1008)).

1028 Lourenço, P. B. Recent Advances in Masonry Structures: Micromodelling and Homogenisation. In
1029 *Multiscale Modeling in Solid Mechanics*, Computational and Experimental Methods in Structures.
1030 Imperial College Press, 3:251–94, 2009, DOI: <https://doi.org/10.1142/p604>.

1031 Lourenço, Paulo B., René De Borst, and Jan G. Rots. A Plane Stress Softening Plasticity Model for
1032 Orthotropic Materials. *International Journal for Numerical Methods in Engineering* **40** (21):
1033 4033–57, 1997, DOI: [https://doi.org/10.1002/\(SICI\)1097-0207\(19971115\)40:21<4033::AID-](https://doi.org/10.1002/(SICI)1097-0207(19971115)40:21<4033::AID-NME248>3.0.CO;2-0)
1034 [NME248>3.0.CO;2-0](https://doi.org/10.1002/(SICI)1097-0207(19971115)40:21<4033::AID-NME248>3.0.CO;2-0).

1035 Lourenço, Paulo B., and Jan G. Rots. Multisurface Interface Model for Analysis of Masonry
1036 Structures.” *Journal of Engineering Mechanics* **123** (7): 660–68, 1997, DOI:
1037 [https://doi.org/10.1061/\(ASCE\)0733-9399\(1997\)123:7\(660\)](https://doi.org/10.1061/(ASCE)0733-9399(1997)123:7(660)).

1038 Lubliner, J., J. Oliver, S. Oller, and E. Oñate. A Plastic-Damage Model for Concrete. *International*
1039 *Journal of Solids and Structures* **25** (3): 299–326, 1989, DOI: [https://doi.org/10.1016/0020-](https://doi.org/10.1016/0020-7683(89)90050-4)
1040 [7683\(89\)90050-4](https://doi.org/10.1016/0020-7683(89)90050-4).

1041 Macorini, L., and B. A. Izzuddin. A Non-Linear Interface Element for 3D Mesoscale Analysis of Brick-
1042 Masonry Structures. *International Journal for Numerical Methods in Engineering* **85** (12): 1584–
1043 1608, 2011, DOI: <https://doi.org/10.1002/nme.3046>.

1044 Macorini, L., and B. A. Izzuddin. Nonlinear Analysis of Unreinforced Masonry Walls under Blast
1045 Loading Using Mesoscale Partitioned Modeling. *Journal of Structural Engineering* **140** (8), 2014,
1046 DOI: [https://doi.org/10.1061/\(ASCE\)ST.1943-541X.0000931](https://doi.org/10.1061/(ASCE)ST.1943-541X.0000931).

1047 Macorini, L., and B.A. Izzuddin. Nonlinear Analysis of Masonry Structures Using Mesoscale
1048 Partitioned Modelling. *Advances in Engineering Software* **60–61** (June): 58–69, 2013, DOI:
1049 <https://doi.org/10.1016/j.advengsoft.2012.11.008>.

1050 Malomo, Daniele, Rui Pinho, and Andrea Penna. Using the Applied Element Method for Modelling
1051 Calcium Silicate Brick Masonry Subjected to In-Plane Cyclic Loading. *Earthquake Engineering*
1052 *& Structural Dynamics* **47** (7): 1610–30, 2018, DOI: <https://doi.org/10.1002/eqe.3032>.

1053 Meguro, K., and H. Tagel-Din. Applied Element Method for Structural Analysis: Theory and
1054 Application for Linear Materials. *JSCE Structural Engineering/Earthquake Engineering* **17** (1):
1055 21–35, 2000.

1056 Milani, G., P.B. Lourenço, and A. Tralli. Homogenised Limit Analysis of Masonry Walls, Part II:
1057 Structural Examples. *Computers & Structures* **84** (3–4): 181–95, 2006, DOI:
1058 <https://doi.org/10.1016/j.compstruc.2005.09.004>.

1059 Milani, Gabriele. 3D Upper Bound Limit Analysis of Multi-Leaf Masonry Walls. *International Journal*
1060 *of Mechanical Sciences* **50** (4): 817–36, 2008, DOI:
1061 <https://doi.org/https://doi.org/10.1016/j.ijmecsci.2007.11.003>.

1062 Milani, Gabriele, PB Lourenço, and Antonio Tralli. Homogenization Approach for the Limit Analysis

1063 of Out-of-Plane Loaded Masonry Walls. *Journal of Structural Engineering* **132** (10): 1650–63,
1064 2006, DOI: [https://doi.org/10.1061/\(ASCE\)0733-9445\(2006\)132:10\(1650\)](https://doi.org/10.1061/(ASCE)0733-9445(2006)132:10(1650)).

1065 Milani, Gabriele, and Antonio Tralli. Simple SQP Approach for Out-of-Plane Loaded Homogenized
1066 Brickwork Panels, Accounting for Softening.” *Computers & Structures* **89** (1–2): 201–15, 2011,
1067 DOI: <https://doi.org/10.1016/j.compstruc.2010.09.005>.

1068 Nard, H. Le, and P. Bailly. Dynamic Behaviour of Concrete: The Structural Effects on Compressive
1069 Strength Increase.” *Mechanics of Cohesive-Frictional Materials* **5** (6): 491–510, 2000, DOI:
1070 [https://doi.org/10.1002/1099-1484\(200008\)5:6<491::AID-CFM106>3.0.CO;2-R](https://doi.org/10.1002/1099-1484(200008)5:6<491::AID-CFM106>3.0.CO;2-R).

1071 NZS1170. Structural Design Actions. Part 5: Earthquake Actions. Standards New Zealand, 2004.

1072 Otero, F., S. Oller, X. Martinez, and O. Salomón. Numerical Homogenization for Composite Materials
1073 Analysis. Comparison with Other Micro Mechanical Formulations. *Composite Structures* **122**
1074 (April): 405–16, 2015, DOI: <https://doi.org/10.1016/j.compstruct.2014.11.041>.

1075 Pandey, A K, Ram Kumar, D K Paul, and D N Triखा. Non-Linear Response of Reinforced Concrete
1076 Containment Structure under Blast Loading. *Nuclear Engineering and Design* **236** (9): 993–1002,
1077 2006, DOI: <https://doi.org/https://doi.org/10.1016/j.nucengdes.2005.09.015>.

1078 Pantò, B, F Cannizzaro, I Calì, and P B Lourenço. Numerical and Experimental Validation of a 3D
1079 Macro-Model for the In-Plane and Out-Of-Plane Behavior of Unreinforced Masonry Walls.
1080 *International Journal of Architectural Heritage* **11** (7): 946–64, 2017, DOI:
1081 <https://doi.org/10.1080/15583058.2017.1325539>.

1082 Pau, Annamaria, and Patrizia Trovalusci. Block Masonry as Equivalent Micropolar Continua: The Role
1083 of Relative Rotations. *Acta Mechanica* **223** (7): 1455–71, 2012, DOI:
1084 <https://doi.org/10.1007/s00707-012-0662-8>.

1085 Pereira, João M., José Campos, and Paulo B. Lourenço. Masonry Infill Walls under Blast Loading
1086 Using Confined Underwater Blast Wave Generators (WBWG). *Engineering Structures* **92**: 69–
1087 83, 2015, DOI: <https://doi.org/10.1016/j.engstruct.2015.02.036>.

1088 Pereira, João M., and Paulo B. Lourenço. Experimental Characterization of Masonry and Masonry
1089 Components at High Strain Rates. *Journal of Materials in Civil Engineering*, **29** (2), 2016a, DOI:
1090 [https://doi.org/10.1061/\(ASCE\)MT.1943-5533.0001755](https://doi.org/10.1061/(ASCE)MT.1943-5533.0001755).

1091 Pereira, João M., and Paulo B. Lourenço. Experimental Bond Behaviour of GFRP and Masonry Bricks
1092 under Impulsive Loading. *Materials and Structures* **49** (11): 4799–4811, 2016b, DOI:
1093 <https://doi.org/10.1617/s11527-016-0826-4>.

1094 Petracca, Massimo, Luca Pelà, Riccardo Rossi, Sergio Oller, Guido Camata, and Enrico Spacone.
1095 Regularization of First Order Computational Homogenization for Multiscale Analysis of Masonry
1096 Structures. *Computational Mechanics* **57** (2): 257–76, 2016, DOI: [https://doi.org/10.1007/s00466-](https://doi.org/10.1007/s00466-015-1230-6)
1097 [015-1230-6](https://doi.org/10.1007/s00466-015-1230-6).

1098 Pontiroli, Christophe, Alain Rouquand, and Jacky Mazars. Predicting Concrete Behaviour from Quasi-
1099 Static Loading to Hypervelocity Impact. *European Journal of Environmental and Civil*
1100 *Engineering* **14** (6–7): 703–27, 2010, DOI: <https://doi.org/10.1080/19648189.2010.9693259>.

1101 Quagliarini, E., G. Maracchini, and F. Clementi. Uses and Limits of the Equivalent Frame Model on
1102 Existing Unreinforced Masonry Buildings for Assessing Their Seismic Risk: A Review. *Journal*
1103 *of Building Engineering* **10** (March): 166–82, 2017, DOI:
1104 <https://doi.org/10.1016/j.jobe.2017.03.004>.

1105 Rafsanjani, S. Hashemi, P.B. Lourenço, and N. Peixinho. Implementation and Validation of a Strain
1106 Rate Dependent Anisotropic Continuum Model for Masonry. *International Journal of Mechanical*
1107 *Sciences* **104**: 24–43, 2015a, DOI: <https://doi.org/10.1016/j.ijmecsci.2015.10.001>.

1108 Rafsanjani, S. Hashemi, P.B. Lourenço, and N. Peixinho. Dynamic Interface Model for Masonry Walls
1109 Subjected to High Strain Rate Out-of-Plane Loads. *International Journal of Impact Engineering*
1110 **76** (February): 28–37, 2015b, DOI: <https://doi.org/10.1016/j.ijimpeng.2014.09.002>.

1111 Rafsanjani, Seyedbrahim. High Strain Rate Constitutive Modeling for Historical Structures Subjected
1112 to Blast Loading, PhD, University of Minho, 2015, from: <http://hdl.handle.net/1822/38459>.

1113 Reccia, Emanuelle, L. Leonetti, Patrizia Trovalusci, and Antonella Cecchi. A Multiscale/Multidomain
1114 Model for the Failure Analysis of Masonry Walls: A Validation with a Combined FEM/DEM
1115 Approach. *International Journal for Multiscale Computational Engineering* **16** (4): 325–43, 2018,
1116 DOI: <https://doi.org/10.1615/IntJMCompEng.2018026988>.

1117 Roca, Pere, Miguel Cervera, Giuseppe Gariup, and Luca Pelà. Structural Analysis of Masonry
1118 Historical Constructions. Classical and Advanced Approaches. *Archives of Computational*

1119 *Methods in Engineering* **17** (3): 299–325, 2010, DOI: [https://doi.org/10.1007/s11831-010-9046-](https://doi.org/10.1007/s11831-010-9046-1)
1120 1.

1121 Roca, Pere, Miguel Cervera, Luca Pelà, Roberto Clemente, and Michele Chiumenti. Continuum FE
1122 Models for the Analysis of Mallorca Cathedral. *Engineering Structures* **46** (January): 653–70,
1123 2013, DOI: <https://doi.org/10.1016/j.engstruct.2012.08.005>.

1124 Rots, J.G., P. Nauta, G. Kusters, and J. Blaauwendraad. Smearred Crack Approach and Fracture
1125 Localization in Concrete. *Heran* **30**: 1–47, 1985.

1126 Sarhosis, Vasilis, Konstantinos Tsavdaridis, and Ioannis Giannopoulos. Discrete Element Modelling
1127 (DEM) for Masonry Infilled Steel Frames with Multiple Window Openings Subjected to Lateral
1128 Load Variations. *The Open Construction and Building Technology Journal* **8** (1): 93–103, 2014,
1129 DOI: <https://doi.org/10.2174/1874836801408010093>.

1130 Sejnoha, J., M. Sejnoha, J. Zeman, J. Sykora, and J. Vorel. A Mesoscopic Study on Historic Masonry.
1131 *Structural Engineering & Mechanics* **30** (1): 99–117, 2008, DOI:
1132 <https://doi.org/10.12989/sem.2008.30.1.099>.

1133 Silva, Luís C., Paulo B. Lourenço, and Gabriele Milani. Rigid Block and Spring Homogenized Model
1134 (HRBSM) for Masonry Subjected to Impact and Blast Loading. *International Journal of Impact*
1135 *Engineering* **109**: 14–28, 2017a, DOI: <https://doi.org/10.1016/j.ijimpeng.2017.05.012>.

1136 Silva, Luís C., Paulo B. Lourenço, and Gabriele Milani. Nonlinear Discrete Homogenized Model for
1137 Out-of-Plane Loaded Masonry Walls.” *Journal of Structural Engineering* **143** (9): 4017099. ,
1138 2017b, DOI: [https://doi.org/10.1061/\(ASCE\)ST.1943-541X.0001831](https://doi.org/10.1061/(ASCE)ST.1943-541X.0001831).

1139 Silva, Luís C., Paulo B. Lourenço, and Gabriele Milani. Derivation of the Out-of-Plane Behaviour of
1140 Masonry through Homogenization Strategies: Micro-Scale Level. *Computers and Structures* **209**:
1141 30–43, 2018, DOI: <https://doi.org/https://doi.org/10.1016/j.compstruc.2018.08.013>.

1142 Silva, Luís C, Nuno Mendes, Paulo B Lourenço, and Jason Ingham. Seismic Structural Assessment of
1143 the Christchurch Catholic Basilica, New Zealand. *Structures* **15**: 115–30, 2018, DOI:
1144 <https://doi.org/https://doi.org/10.1016/j.istruc.2018.06.004>.

1145 Sinha, B. P. A Simplified Ultimate Load Analysis of Laterally-Loaded Model Orthotropic Brickwork
1146 Panels of Low Tensile Strength. *Structural Engineering ASCE* **56B** (4): 81–84, 1978.

1147 Sluys, L.J., and R. De Borst. Computational Modeling of Impact Tests on Steel Fibre Reinforced
1148 Concrete Beams.” *Heron* 37 (4): 3–15, 1992.

1149 Spahn, J., H. Andrä, M. Kabel, and R. Müller. A Multiscale Approach for Modeling Progressive
1150 Damage of Composite Materials Using Fast Fourier Transforms. *Computer Methods in Applied
1151 Mechanics and Engineering* **268** (January): 871–83, 2014, DOI:
1152 <https://doi.org/10.1016/j.cma.2013.10.017>.

1153 Taliercio, Alberto. Closed-Form Expressions for the Macroscopic in-Plane Elastic and Creep
1154 Coefficients of Brick Masonry. *International Journal of Solids and Structures* **51** (17): 2949–63,
1155 2014, DOI: <https://doi.org/10.1016/j.ijsolstr.2014.04.019>.

1156 Theodossopoulos, Dimitris, and Braj Sinha. A Review of Analytical Methods in the Current Design
1157 Processes and Assessment of Performance of Masonry Structures. *Construction and Building
1158 Materials* **41** (April): 990–1001, 2013, DOI: <https://doi.org/10.1016/j.conbuildmat.2012.07.095>.

1159 Tomažević, M. *Earthquake-Resistant Design of Masonry Buildings*. Vol. 1. World Scientific, 1999.

1160 Trovalusci, Patrizia, Martin Ostoja-Starzewski, Maria Laura De Bellis, and Agnese Murralli. Scale-
1161 Dependent Homogenization of Random Composites as Micropolar Continua. *European Journal
1162 of Mechanics - A/Solids* **49**: 396–407, 2015, DOI:
1163 <https://doi.org/https://doi.org/10.1016/j.euromechsol.2014.08.010>.

1164 Wu, Chengqing, Hong Hao, and Yong Lu. Dynamic Response and Damage Analysis of Masonry
1165 Structures and Masonry Infilled RC Frames to Blast Ground Motion. *Engineering Structures* **27**
1166 (3): 323–33, 2005, DOI: <https://doi.org/10.1016/j.engstruct.2004.10.004>.

1167 Zapata, Brian J., and David Weggel. Collapse Study of an Unreinforced Masonry Bearing Wall
1168 Building Subjected to Internal Blast Loading. *Journal of Performance of Constructed Facilities*
1169 **22** (2): 92–100, 2008, DOI: [https://doi.org/10.1061/\(ASCE\)0887-3828\(2008\)22:2\(92\)](https://doi.org/10.1061/(ASCE)0887-3828(2008)22:2(92)).

1170 Zucchini, A, and PB. Lourenço. A Micro-Mechanical Model for the Homogenisation of Masonry.
1171 *International Journal of Solids and Structures* **39** (12): 3233–55, 2002, DOI:
1172 [https://doi.org/10.1016/S0020-7683\(02\)00230-5](https://doi.org/10.1016/S0020-7683(02)00230-5).

1173

